

# **SPECTRAL DOMAIN OPTICAL COHERENCE TOMOGRAPHY IN GLAUCOMA: QUALITATIVE AND QUANTITATIVE ANALYSIS OF THE OPTIC NERVE HEAD AND RETINAL NERVE FIBER LAYER (AN AOS THESIS)**

---

BY Teresa C. Chen MD

## **ABSTRACT**

*Purpose:* To demonstrate that video-rate spectral domain optical coherence tomography (SDOCT) can qualitatively and quantitatively evaluate optic nerve head (ONH) and retinal nerve fiber layer (RNFL) glaucomatous structural changes. To correlate quantitative SDOCT parameters with disc photography and visual fields.

*Methods:* SDOCT images from 4 glaucoma eyes (4 patients) with varying stages of open-angle glaucoma (ie, early, moderate, late) were qualitatively contrasted with 2 age-matched normal eyes (2 patients). Of 61 other consecutive patients recruited in an institutional setting, 53 eyes (33 patients) met inclusion/exclusion criteria for quantitative studies. Images were obtained using two experimental SDOCT systems, one utilizing a superluminescent diode and the other a titanium:sapphire laser source, with axial resolutions of about 6  $\mu\text{m}$  and 3  $\mu\text{m}$ , respectively.

*Results:* Classic glaucomatous ONH and RNFL structural changes were seen in SDOCT images. An SDOCT reference plane 139  $\mu\text{m}$  above the retinal pigment epithelium yielded cup-disc ratios that best correlated with masked physician disc photography cup-disc ratio assessments. The minimum distance band, a novel SDOCT neuroretinal rim parameter, showed good correlation with physician cup-disc ratio assessments, visual field mean deviation, and pattern standard deviation (*P* values range, .0003-.024). RNFL and retinal thickness maps correlated well with disc photography and visual field testing.

*Conclusions:* To our knowledge, this thesis presents the first comprehensive qualitative and quantitative evaluation of SDOCT images of the ONH and RNFL in glaucoma. This pilot study provides basis for developing more automated quantitative SDOCT-specific glaucoma algorithms needed for future prospective multicenter national trials.

*Trans Am Ophthalmol Soc 2009;107:254-281*

## **INTRODUCTION**

---

### **THE PROBLEM: GLAUCOMA**

Glaucoma is the second-leading cause of blindness in the world, affecting more than 2.5 million people in the United States.<sup>1-3</sup> Owing to the rapidly aging population, the number with open-angle glaucoma will increase by 50% to 3.36 million in 2020. It is estimated that more than 130,000 people are legally blind from the disease.<sup>4</sup> Open-angle glaucoma alone has an overall prevalence of approximately 1.55%<sup>4</sup> to 3%<sup>5,6</sup> and is the leading cause of blindness among African Americans.<sup>7-11</sup> The prevalence ranges from 1.2% in African Americans between the ages of 40 and 49 years to 11.3% in those 80 years and older.<sup>10</sup> These numbers may be underestimating the true prevalence of glaucoma, since up to half of patients with glaucoma, even in developed countries, are undiagnosed and since a large proportion of glaucoma patients who are eligible for registration as legally blind remain unregistered.<sup>12-16</sup>

### **WHY THERE IS A NEED FOR BETTER IMAGING OF THE OPTIC NERVE HEAD AND THE RETINAL NERVE FIBER LAYER**

Because of the large numbers of people glaucoma affects, there is clearly a need to develop a better instrument or method that can diagnose glaucoma earlier and more objectively. Since glaucoma causes irreversible loss of vision, the main goal of glaucoma management is to diagnose this initially asymptomatic disease as early as possible. Once glaucoma is diagnosed, treatment can be initiated to either stop or slow down further permanent vision loss. Another reason for a late diagnosis is that patients are usually not symptomatic until the disease is in its advanced stages, since glaucoma does not cause pain and usually causes loss of peripheral vision first, before central vision. Another obstacle in diagnosing glaucoma is that the current standard clinical methods of glaucoma diagnosis, which include the visual field test, rely not only on the subjective test response of the patient but also on the subjective interpretation of this test by the physician. These subjective methods, which are currently the clinical "gold standards," can diagnose glaucomatous vision loss only after up to 40% of the nerve tissue is lost irreversibly.<sup>17-20</sup> Because of the need to diagnose glaucoma not only earlier but also in a more objective manner, imaging methods such as scanning laser polarimetry, confocal scanning laser ophthalmoscopy, and time domain optical coherence tomography (OCT) have been developed in an attempt to measure objectively and quantitatively changes in both the optic nerve head (ONH) and the retinal nerve fiber layer (RNFL), both of which undergo structural changes with glaucoma.

Early detection of glaucoma has focused on evaluation of the ONH and the RNFL, because both the RNFL and the ONH can be imaged and have been shown to undergo structural changes prior to clinically detectable visual field loss. In theory, RNFL analysis may be more sensitive than ONH evaluation, because OCT has shown thinning of the nerve fiber layer due to aging without detectable changes in the ONH appearance.<sup>21</sup> Nerve fiber layer thinning is seen in glaucoma, because it is directly correlated with loss of ganglion cells, which is assumed to be a primary event in glaucomatous damage.<sup>22</sup> It has been suggested that thinning of the nerve fiber layer, as determined by subjective physician assessment of red-free RNFL photos, can even occur up to 6 years prior to clinically

From the Massachusetts Eye and Ear Infirmary, Glaucoma Service, Harvard Medical School, Department of Ophthalmology, Boston, Massachusetts.

detectable loss of vision.<sup>23</sup> In practice, ONH imaging using the current commercially available imaging modalities of scanning laser polarimetry, confocal scanning laser ophthalmoscopy, and time domain OCT may correlate better with actual glaucoma disease compared to RNFL parameters obtained by these same imaging devices.<sup>24</sup> The Ocular Hypertension Treatment Study (OHTS), which included 1,636 ocular hypertension patients and which is the largest prospective multicenter trial that evaluated these at-risk patients, showed that 51.8% of at-risk patients (87 of 168 eyes) can be diagnosed as having glaucoma based on progressive ONH changes that were determined by subjective physician assessment of serial stereo disc photos taken over a 5-year follow-up period. These 87 eyes developed ONH changes prior to visual field loss.<sup>25</sup> Because RNFL thinning and ONH changes are irreversible, early diagnosis is essential. If an imaging instrument were developed that could objectively detect these RNFL and ONH changes years before visual field loss, then medical or surgical treatments could possibly be initiated years earlier than current subjective diagnostic techniques allow. Treatment may then slow down or stop progressive RNFL axonal degeneration and irreversible vision loss. Population surveys also suggest the need for better diagnostic instruments, in that less than 50% of those with glaucomatous visual field loss have received an appropriate diagnosis or treatment.<sup>12-14</sup>

A better imaging instrument that can objectively measure ONH and RNFL parameters would also be useful for the monitoring and treatment of glaucoma patients. Although many studies in glaucoma imaging have focused on early diagnosis, the task of detecting disease progression is perhaps equally important. Since glaucoma is a lifelong disease that evolves over decades, detecting the progression of the disease requires longitudinal follow-up.<sup>26</sup> If ophthalmologists had a better objective imaging device and were able to objectively detect ONH changes or RNFL thinning prior to further loss of vision, more aggressive treatment and lowering of the intraocular pressure may prevent patients from developing further loss of vision.

### **LIMITATIONS OF THE CURRENT APPROACHES USED TO EVALUATE ONH CHANGES AND RNFL THINNING**

The need for better methods to objectively evaluate or image the ONH and RNFL is apparent when considering the limitations of current subjective clinical methods to evaluate the ONH and the RNFL.

Although stereo disc photography of the ONH remains part of the cornerstone of glaucoma diagnosis, evaluation of these photos is still subjective. Since glaucoma is defined as a characteristic optic neuropathy with corresponding visual field loss with elevated intraocular pressure as its main risk factor, careful assessment of optic nerve photos and visual field tests is integral for accurate glaucoma diagnosis. Stereo photos of the optic nerve are still considered the “gold standard” assessment of glaucomatous optic neuropathy, and stereophotograph grading still has the largest area under the receiver operating curves compared to best parameters from HRTII, GDxVCC, and Stratus OCT.<sup>24,27</sup> However, a standardized objective method to evaluate the ONH is needed, because there is significant variability even between glaucoma specialists in the evaluation of the cup-disc ratio from stereo disc photos. Studies have demonstrated that 4% to 19% of cup-disc estimates made by 2 different glaucoma specialists differed by 0.2 disc diameters or more.<sup>28-32</sup> Visual field evaluation is even more subjective than stereo disc photo assessment, because 86% of visual field abnormalities could not be replicated on retesting in a study of 1,637 patients.<sup>33</sup>

Red-free photography of the RNFL also has its limitations, in that its evaluation is also still subjective. Photography in red-free light enhances the contrast of the RNFL, and the technique for such photography has reached an advanced state of development. In a few centers it is done routinely; however, it is considered labor-intensive.<sup>26</sup> Another limitation of red-free photography is the subjectivity of the quantitative analysis and the dependence on the physician. However, it has increased our awareness of the usefulness, even the critical importance, of nerve fiber layer evaluation in patients with glaucoma.<sup>26</sup> Studies with red-free photography have shown that nerve fiber layer defects may be present even 6 years before documented visual field loss.<sup>23</sup>

Because of the need to diagnose glaucoma not only earlier but also in a more objective manner, 3 main imaging methods have been developed: scanning laser polarimetry, confocal scanning laser ophthalmoscopy, and OCT. Each of these imaging technologies also has its limitations.

Scanning laser polarimetry technology (GDxFCC and VCC; formerly Laser Diagnostic Technologies Inc, San Diego, California; currently Carl Zeiss Meditec Inc, Dublin, California) is ultimately limited by the fact that it does not directly measure RNFL thickness. It determines RNFL thickness indirectly by measuring the phase retardation of the birefringent RNFL. The birefringence of the RNFL is due to anisotropic structures, including microtubules and axon membranes dispersed in an oriented manner.<sup>34,35</sup> Polarized light from the GDx machine propagates through the RNFL and acquires a phase retardation in the birefringent RNFL in proportion to the RNFL thickness. Then most of the incident polarized light is reflected back from layers beneath the RNFL, thus double-passing the full thickness of the nerve fiber layer.<sup>36</sup> This double-pass phase retardation (DPPR) measurement is then divided by a constant birefringence value in order to calculate RNFL thickness [formula:  $DPPR = \text{birefringence} \times 2 \text{ RNFL thickness} \times (2\pi/\text{wavelength})$ ]. The RNFL thickness measurement with scanning laser polarimetry is incorrect, because it assumes a constant birefringence value for everyone and also assumes a constant birefringence value throughout the retina. Using the first polarization-sensitive OCT machine that enabled in vivo birefringence measurements of the human RNFL, Cense and colleagues<sup>37</sup> found that birefringence of the RNFL varies not only with location but also from person to person, invalidating an extrapolation of phase retardation to RNFL thickness using a constant birefringence value. Using indirect methods to calculate RNFL birefringence values, Huang and colleagues<sup>38</sup> also confirmed that birefringence of the RNFL varies with location in the eye and is not constant. In light of these 2 studies and the above DPPR formula, GDxVCC RNFL thickness values that are calculated using a constant birefringence value may be associated with RNFL thickness values that are off by up to around 30%. The introduction of the GDx with variable corneal compensator (GDxVCC) in 2003 did allow for better phase retardation measurements, as artifact can be created from the birefringent cornea; however, the GDxVCC still assumes a constant birefringence value for all scans. Previous studies evaluating sensitivity reported values ranging from 74% to 94% and specificity values from 74% to 91% for detecting glaucoma.<sup>39-41</sup>

Confocal scanning laser tomography (HRT/Heidelberg Retina Tomograph, Heidelberg Instruments, Heidelberg, Germany, and TopSS, Laser Diagnostic Technologies Inc, San Diego, California) produces a 3-dimensional (3D) topographic representation of the ONH but is ultimately limited by its lower resolution (ie, 300- $\mu\text{m}$  axial resolution for the HRT3) and ability to depict only surface topography. HRT evaluation of the optic disc and peripapillary area has been reported to be more sensitive in detecting glaucoma than the pre-VCC GDx.<sup>42</sup> The confocal scanning laser tomography method provides sectioning capability by use of a short confocal parameter. Owing to the low numerical aperture of the human eye, the depth-sectioning capability is approximately 200 to 300  $\mu\text{m}$ . This is what limits this modality to depicting only surface topography. Correct measurement of disc topography and associated summary indices is also dependent on correct placement of the contour line (optic disc margin) by the operator, as well as upon intraocular pressure and cardiac pulsations.<sup>22</sup> Since HRT is limited to ONH surface topography, confocal scanning laser tomographs (HRT) cannot measure RNFL thickness directly, but can only estimate RNFL thickness by calculating the difference between the retinal surface and a set reference plane 50  $\mu\text{m}$  below the surface of the retina temporal to the ONH. Most recent clinical studies have shown sensitivities ranging from 40% to 86% and specificities ranging from 54% to 93% with the HRT3.<sup>43-46</sup>

Time domain OCT (Stratus OCT 3, Carl Zeiss Meditec Inc, Dublin, California) can image both the ONH and the RNFL thickness. Recent results from the Advanced Imaging for Glaucoma Study (AGIS) showed that the best RNFL parameters to diagnose “perimetric glaucoma” (ie, glaucoma based on abnormal visual field testing and glaucomatous ONH abnormalities) were the overall, superior quadrant or inferior quadrant RNFL thickness values, with sensitivities around 72.9% and specificities of 93.7% based on the fifth percentile cutoff criteria.<sup>47</sup> This is based on analysis of 89 normal and 89 age-matched perimetric glaucoma patients. Older Stratus OCT3 studies showed sensitivities between 65% and  $\geq 90\%$  for specificities 71.6% to  $\geq 95\%$ <sup>48-57</sup> using best ONH or RNFL thickness parameters.

However, recent studies suggest that the receiver operating characteristic curves were similar for GDxVCC, HRTII, and Stratus OCT.<sup>24,58</sup> Potential advantages of spectral domain OCT over these older technologies are its faster acquisition times and its higher resolutions. Because the Stratus OCT takes about 1.28 seconds to image the optic nerve, motion artifact is introduced, necessitating realignment of A-lines. Therefore, the Stratus OCT3 does not show true ONH topography. Even with the ultrahigh-resolution time domain OCT, slower acquisition speeds still necessitate realignment of A-lines.<sup>59</sup> With the ultrahigh acquisition speeds of spectral domain OCT, realignment of A-lines within a single image becomes unnecessary.<sup>60</sup> Spectral domain OCT is also potentially better than confocal scanning laser ophthalmoscopy (HRT) in that it is not limited to measuring only surface topography but also enables higher-resolution imaging (ie, 2  $\mu\text{m}$  axial resolution for spectral domain OCT<sup>60-63</sup> compared to the 300  $\mu\text{m}$  axial resolution for the HRT).

All 3 objective imaging methods (ie, GDx, HRT, and time domain OCT) have not demonstrated better sensitivity and specificity than current clinical techniques, which include stereo disc photography and visual field testing, in the detection of glaucomatous damage.<sup>27,64</sup> Despite this, there is still reason to believe that imaging devices may be capable of predicting the onset of glaucoma prior to clinically detectable visual field loss. In retrospective studies or post hoc analysis of prospective studies that used OCT (OCT2, Carl Zeiss Meditec Inc, Dublin, California), confocal scanning laser ophthalmoscopy (older version and HRT3), and scanning laser polarimetry (GDxFCC, Laser Diagnostic Technologies Inc, San Diego, California), certain baseline parameters were associated with the development of open-angle glaucoma in either glaucoma suspect or ocular hypertension patients.<sup>65-69</sup> However, of these 3 imaging technologies, OCT has the greatest potential for the evaluation of glaucoma patients, because it is the only technology that can both image the ONH and directly determine RNFL thickness.

## DEVELOPMENT OF TIME DOMAIN AND SPECTRAL DOMAIN OCT

Since its introduction by James Fujimoto, PhD, at the Massachusetts Institute of Technology almost 15 years ago, time domain OCT<sup>70</sup> has become an important instrument for the practicing ophthalmologist. Clinical studies utilizing time domain OCT were initially conducted by Joel Schuman, MD, and Carmen Puliafito, MD, MBA, at Tufts University. It is often said that OCT is analogous to ultrasound; however, instead of using sound, it utilizes light. Images are created based on the different reflectivity of different ocular structures. Similar to an A-scan in ultrasound technology, an A-line in OCT represents a 1-dimensional unit of data. In ultrasound, many A-scans can be combined to create a B-scan 2-dimensional (2D) image. In OCT, many A-lines can be combined to create a 2D OCT image. However, unlike ultrasound using sound, light travels so fast that one needs a fundamentally different way to process this information. The typical setup in a time domain OCT machine (Figure 1) shows light being emitted from a superluminescent diode (SLD) light source. The light goes through the beam splitter to the eye and a reference mirror. As the light comes back from the eye and the reference mirror, the interference pattern is processed by a photodetector whose data is then used to create a 2D image. Until late 2006, all commercially available US Food and Drug Administration (FDA)-approved instruments, including the Stratus OCT (Carl Zeiss Meditec Inc, Dublin, California) and the Visante (Carl Zeiss Meditec Inc), were based on time domain OCT. For posterior segment imaging, a typical time domain Stratus OCT scan can be acquired in 1.28 seconds and can produce a 2D image with an axial resolution of about 10  $\mu\text{m}$ . Therefore, limitations of time domain OCT include slow acquisition speed and lower resolution.

To improve resolution, ultrahigh-resolution time domain OCT imaging was developed, and axial resolutions of about 3  $\mu\text{m}$  were achieved.<sup>71-74</sup> Ultrahigh-resolution time domain OCT imaging, however, traded ultrahigh resolution for slower acquisition speeds, and comparable 2D images would take several seconds to obtain.

To achieve simultaneous ultrahigh resolutions with ultrahigh acquisition speeds, a fundamentally new technology was developed, and it is called video-rate spectral domain OCT or Fourier domain OCT. Although the concept of a spectrometer has been known for decades and although earlier iterations of spectral domain OCT machines took too long to obtain and process an image to be clinically useful,<sup>75</sup> the first prototype video-rate spectral domain OCT machine that could obtain and display images in effective real-time was

built by Johannes de Boer, PhD, at the Massachusetts General Hospital Wellman Center for Photomedicine.<sup>60,61,76-79</sup> Clinical studies utilizing video-rate spectral domain OCT were first conducted by Teresa Chen, MD, at the Massachusetts Eye and Ear Infirmary (deBoer JF, American Glaucoma Society Meeting, 2004, Abstract; Chen TC, ARVO Meeting, 2006, Abstract).<sup>60,61,76-78,80-86</sup> The term “video-rate” is used to describe this first clinically useful spectral domain OCT machine, because “video-rate” means that at least 30 frames can be acquired per second. Because the eye integrates each image it receives over a certain time interval and is not an instantaneous detector, televisions or “videos” display images at 30 frames per second so that the eye will “see” a continuous motion on the screen. If the television or computer screen were to display images at, for example, 20 frames per second, our brain would realize that the motion is discrete. The term “spectral domain OCT” is preferred over “Fourier domain OCT,” because the fundamental difference between time domain and spectral domain OCT is the spectrometer, which is how the light is processed as it comes back from the eye and the reference mirror (Figure 2). Instead of the light from the eye and reference mirror being processed by a photodetector, it is processed by a spectrometer, which is more efficient than a photodetector and is similar to having thousands of photodetectors acting in parallel. The spectrometer is composed of the transmission grating and the air-spaced focusing lens. Although this information is then ultimately analyzed using Fourier transform in order to create the image, hence the term “Fourier domain OCT,” the spectrometer is what ultimately enables ultrahigh resolutions with ultrahigh acquisition speeds.

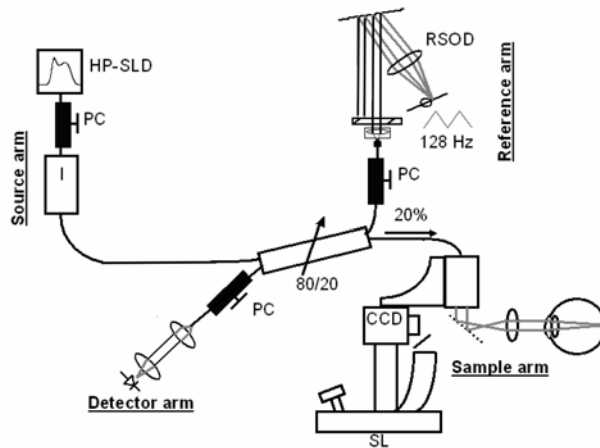


**FIGURE 1**

Schematic of a time domain optical coherence tomography setup. CCD, charge coupled device; HP-SLD, high-power superluminescent diode; PC, polarization controllers; RSOD, delay line; SL, slit lamp.

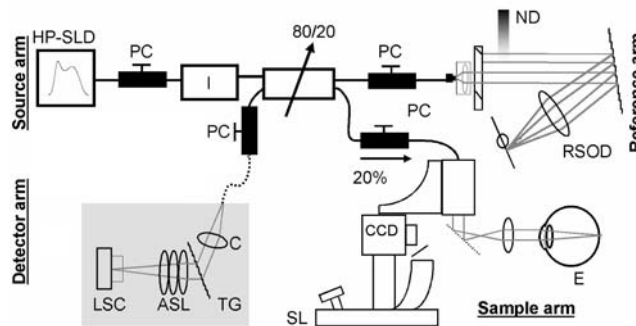


**FIGURE 2**

Schematic of the spectral domain optical coherence tomography (OCT) setup that was used for in vivo measurements. ASL, air spaced lens; C, collimator; CCD, charge coupled device; E, eye; HP-SLD, high-power superluminescent diode; LSC, line scan camera; ND, neutral density filter; PC, polarization controllers; RSOD, delay line; SL, slit lamp; TG, transmission grating.

Spectral domain OCT allows for unprecedented simultaneous ultrahigh speed and ultrahigh resolution ophthalmic imaging without a loss in image quality, and 2D images can be obtained in 1/29th of a second.<sup>76,77</sup> In contrast to time domain OCT, which may image 400 A-lines per second, spectral domain OCT can image 14,600 to over 29,200 A-lines per second. Although spectral domain OCT can employ either a SLD or a titanium:sapphire (Ti:sapphire) laser source, spectral domain OCT resolutions of about 2 μm can be achieved with the appropriate light source.<sup>60-63</sup> Unlike traditional time domain OCT with 2D data displays, spectral domain OCT can

create 3-dimensional (3D) images as well as videos of large areas of the posterior pole. Other capabilities of spectral domain OCT include imaging of retinal blood flow via Doppler imaging,<sup>78,87</sup> anterior segment imaging that may utilize different light sources,<sup>88-91</sup> and in vivo measurements of human RNFL birefringence by polarization-sensitive OCT.<sup>37,92</sup>

Spectral domain OCT allows for better images, because its fundamentally different detection method is more efficient<sup>79,93</sup> and allows for a 150-fold (21.7 dB) improvement in sensitivity compared to equivalent time domain OCT systems.<sup>76,77</sup> This higher sensitivity allows for faster acquisition speeds and for detection of weaker signals.<sup>60</sup> In a spectral domain OCT setup (Figure 2), a similar SLD source that is used in the time domain Stratus OCT may be used. The light emitted from the source arm passes through a beam splitter such that the light travels to both the reference mirror in the reference arm and the eye in the sample arm. The reflected light coming back from both the reference mirror and the eye interferes, producing interference fringes. The light coming back from different depths in the retina generates fringes with different frequencies, the amplitude of these fringes being proportional to the reflectivity corresponding to each depth. The interference spectrum is analyzed in the detector arm by a spectrometer and is then Fourier transformed to produce a reflectivity depth profile (A-line or A-scan), without the need of a moving reference arm mirror. Because a spectrometer fundamentally increases the acquisition efficiency, this technology is called spectral domain OCT. This more efficient data acquisition technology of spectral domain OCT allows for imaging of the ONH, retina, and blood flow at ultrahigh speeds of 34.1  $\mu\text{sec}$  per A-line. Single images, or B-scans, composed of 1,000 A-lines can be acquired in 34.1 microseconds or 1/29th of a second. This is 73 times faster than the commercially available Stratus OCT, which can take 1.28 seconds to create an image of 512 A-lines.<sup>60</sup> Spectral domain OCT can also achieve axial resolutions of about 2.6  $\mu\text{m}$  in air and 2  $\mu\text{m}$  in the eye.<sup>63</sup>

### **RATIONALE FOR THIS PILOT STUDY OF SPECTRAL DOMAIN OCT AND GLAUCOMA**

A fundamental requirement of any new imaging technology for glaucoma care is the ability of that technology to *qualitatively* depict glaucomatous structural changes consistent with known pathologic changes in glaucoma. In this thesis, we demonstrate how spectral domain OCT can image classic structural changes associated with glaucoma: (1) ONH cupping, (2) “beanpot” cupping, (3) bayoneting of the ONH blood vessels, (4) barring of the circumlinear ONH blood vessels, (5) RNFL thinning, and (6) exposure of second-order blood vessels above the surface of a thinned RNFL.

New algorithms that *quantitatively* evaluate spectral domain OCT 3D ONH images need to be developed and tested, in that the 2 main ONH imaging technologies (ie, HRT and time domain Stratus OCT) evaluate only 2D ONH images. Spectral domain OCT also allows for 3D evaluation of the RNFL and quantitative RNFL thickness maps of large regions of the posterior pole, unlike older RNFL imaging technologies (ie, GDxVCC and time domain Stratus OCT), which display only peripapillary RNFL thickness values in either 1 or 2 dimensions. This thesis proposes new methods to quantitatively evaluate 3D spectral domain OCT data: (1) new spectral domain OCT reference plane for more accurate correlation of automated spectral domain OCT vertical cup-disc ratio calculations with the classic disc photography physician vertical cup-disc ratio assessments; (2) new “minimum distance band” parameter for 3D evaluation of the ONH neuroretinal rim tissue; and (3) RNFL thickness maps and retinal thickness maps of large regions of the posterior pole.

A new spectral domain OCT reference plane is needed, since the current time domain Stratus OCT reference plane (ie, the plane 150  $\mu\text{m}$  above the retinal pigment epithelium [RPE]), which divides the cup from the neuroretinal rim, yields vertical cup-disc ratio assessments that are slightly larger than the vertical cup-disc ratio assessments as determined by clinical examination or standard disc photography. The classic vertical cup-disc ratio assessments by time domain Stratus OCT and clinical ONH examination differ by 0.00 to 0.11, with better correlation in glaucomatous eyes with larger cup-disc ratios.<sup>94-96</sup> Although spectral domain OCT can ultimately determine 3D volume assessments of the ONH and the neuroretinal rim, determination of the most appropriate reference plane is vital in OCT imaging, because most ONH parameters are based on the reference plane. With respect to other ONH imaging modalities that utilize a reference plane, the HRT reference plane (ie, the plane 50  $\mu\text{m}$  below the temporal retinal surface) is different from the Stratus OCT reference plane. Refinement of the HRT reference plane is also needed,<sup>97</sup> but ONH parameters as measured by HRT and Stratus OCT are notably not interchangeable.<sup>98,99</sup> Some studies suggest that HRT cup-disc ratio assessments are similar to disc photography,<sup>100,101</sup> but other studies suggest that these differences are too large to be interchangeable in a clinic setting.<sup>102-104</sup> Unfortunately, many of these studies do not quantify by how much the vertical cup-disc ratio assessments of HRT differ from disc photography and usually merely state that correlation between HRT and disc photography was either good or poor. Because of the potential limitations of the standard 150  $\mu\text{m}$  reference plane used in time domain OCT, a goal of this study is to determine if a different reference plane allows better correlation of spectral domain OCT vertical cup-disc ratio assessments with glaucoma specialists’ cup-disc ratio assessments on fundus photography.

Since an obvious advantage of spectral domain OCT over both time domain OCT and stereo disc photography is the ability to image the ONH in 3D, new spectral domain OCT parameters that quantitatively evaluate the neuroretinal rim tissue in 3D need to be studied in order to supplement the classic 1-dimensional vertical cup-disc ratio assessment. This thesis will study the potential of Povazay’s “minimum distance mapping” as a method to quantify spectral domain OCT ONH images.<sup>105</sup> Povazay and colleagues demonstrated this parameter in 3 patients (ie, one normal subject and 2 glaucoma patients). This thesis redefines this parameter as the “minimum distance band” (MDB),<sup>86</sup> which is the circular band whose outer border or ring is defined by the edge of the RPE and whose inner ring is the ONH surface that has the shortest distance from the RPE edge. This study will demonstrate that this MDB parameter can be reliably determined in a larger sampling of study patients. To assess the clinical relevance of this MDB parameter, the “minimum distance band” will be correlated with traditional clinical parameters (ie, glaucoma specialists’ assessments of vertical cup-disc ratios from disc photos as well as mean deviations and pattern standard deviations from Humphrey visual field testing).

The ability of spectral domain OCT to produce RNFL thickness maps has already been demonstrated in previous publications.<sup>80,86</sup>

For completeness sake, this thesis will again briefly demonstrate how RNFL thickness maps can show good correlation with clinical findings (ie, ONH photography and Humphrey visual field testing). A newer concept, the use of retinal thickness maps of large regions of the peripapillary retina, will also be demonstrated, since retinal thickness maps may potentially better show glaucomatous structural changes than RNFL thickness maps in select patients.

In summary, this thesis will demonstrate that spectral domain OCT images of the ONH and RNFL can *qualitatively* image structural changes that are known to occur with glaucoma. These structural ONH and RNFL changes will be shown in representative eyes with varying stages of glaucoma (eg, early, moderate, and advanced glaucoma). Because the RNFL normally thins with aging, glaucoma RNFL images will be compared to age-matched normals. These spectral domain OCT images of the ONH and RNFL may support the phrase that OCT can often be considered as *in vivo* histology.<sup>106</sup> This study will also evaluate the clinical relevance of new algorithms that *quantitatively* analyze 3D spectral domain OCT data. This pilot study will present a new spectral domain OCT reference plane for better automated cup-disc ratio assessment and from which other future spectral domain OCT parameters can be calculated. In addition, this pilot study demonstrates a new “minimum distance band” parameter for 3D ONH neuroretinal rim evaluation. Where applicable, spectral domain OCT data will be correlated with traditional clinical parameters (ie, glaucoma specialists’ assessments of vertical cup-disc ratios from disc photos as well as mean deviations and pattern standard deviations from Humphrey visual field testing). Quantitative RNFL and retinal thickness maps will also be shown.

## **METHODS**

---

Approvals from both Massachusetts Eye and Ear Infirmary and Massachusetts General Hospital Institutional Review Boards were obtained for all the following protocols. Informed consents were obtained for all volunteers and were in accordance with the Health Insurance Portability and Accountability Act.

Two experimental spectral domain OCT instruments were developed by Johannes de Boer, PhD, at the Massachusetts General Hospital Wellman Center for Photomedicine. For the Massachusetts Eye and Ear Infirmary spectral domain OCT system, the source was a SLD (Superlum, Moscow, Russia) with a full width at half maximum (FWHM) spectral width of 50 nm centered at 840 nm (Figure 2). For the Massachusetts General Hospital Wellman Center spectral domain OCT system, the source was a Ti:sapphire laser (Integral OCT, Femtolasers, Vienna, Austria) with a FWHM spectral width of 140 nm centered at 800 nm. Two-dimensional spectral domain OCT images were obtained in 1/29th of a second. Spectral domain OCT was able to create 3D large area tomographic videos of the ONH and retina in under 10 seconds. The incident optical power in the eye was about 600  $\mu$ W in both cases, well below the American National Standards Institute standards.<sup>107</sup>

Patients were imaged with the Massachusetts General Hospital Ti:sapphire laser source spectral domain OCT system whenever possible. When the study volunteers could not or were not willing to go to the Massachusetts General Hospital Wellman Center for imaging, they were imaged with the Massachusetts Eye and Ear Infirmary SLD spectral domain OCT system. Since normal volunteers A and B were recruited through flyers at the Massachusetts General Hospital, these study volunteers were imaged with the Ti:sapphire system. Since all the other study volunteers were recruited from clinics at the Massachusetts Eye and Ear Infirmary, all of these other patients were imaged with the SLD system.

All patients were examined by a glaucoma specialist (T.C.) and had visual acuity testing, refraction, slit-lamp examination, Goldmann applanation tonometry, gonioscopy, and dilated fundus examination. All study patients had fundus photography (Topcon TRC 50IX fundus camera [Topcon, Tokyo, Japan] or Visucam Pro NM [Carl Zeiss Meditec Inc, Dublin, California]) as well as Humphrey visual field testing (SITA-standard 24-2 strategy, model HFAII series 750i, Carl Zeiss Meditec Inc). A reliable Humphrey visual field test was defined as a test with 33% or less fixation losses, 20% or less false-positives, and 20% or less false-negatives, which were similar reliability indices used in the recent OHTS protocol.<sup>108,109</sup> OHTS investigators felt that having a more stringent criteria of 20% fixation losses would not significantly affect study results but would have unnecessarily reduced study numbers.

Overall eligibility of a subject for this study was based on a medical and ocular history and on a comprehensive eye examination (including standard disc photography and Humphrey visual field testing). One or both eyes of one subject could be enrolled, as long as each eye met the following inclusion and exclusion criteria. These criteria were modified from the Advanced Glaucoma Intervention Study (AGIS), one of the largest multicenter prospective national trials of open-angle glaucoma patients.

Overall inclusion criteria included age between 35 and 85 years, visual acuity score of 56 or better (approximate Snellen equivalent 20/80), ability to cooperate with study procedures and to perform tests reliably, and written informed consent.

Glaucoma patients were recruited from the Massachusetts Eye and Ear Infirmary Glaucoma Service. Inclusion criteria for *open-angle glaucoma patients* were as follows: (1) characteristic glaucomatous visual field changes and (2) corresponding ONH changes characteristic for glaucoma based on both standard stereo slit-lamp examination and review of stereo disc photographs (see paragraph below on “optic disc abnormalities”). Diagnoses of the following types of open-angle glaucoma were included: primary, normal tension, pseudoexfoliation, and pigmentary. Eligibility criteria were modeled after AGIS criteria for open-angle glaucoma (Table 1 from *Controlled Clinical Trials* 1994;15:299-325).

“Optic disc abnormalities” were assessed by the clinical impression of a glaucoma specialist. A disc abnormality must include one or more of the following: excavation, notching, focal or diffuse atrophy of neuroretinal rim area, vertical cup-disc ratio more than 0.6, cup-disc asymmetry between fellow eyes greater than 0.2, or disc hemorrhage. Excavation was defined as undermining of the neuroretinal rim; notching was considered if it involved 2 clock hours; atrophy was defined as neuroretinal rim thinning involving 2 or more clock hours.

Overall exclusion criteria included discernible congenital anomaly of the anterior chamber; eyes with secondary glaucoma; concurrent active eye disease in the study eye that may affect intraocular pressure or its measurement; patients on kidney dialysis; Trans Am Ophthalmol Soc / 107 / 2009

history of previous intraocular surgery (other than laser trabeculoplasty; uncomplicated cataract extraction with posterior chamber intraocular lens; trabeculectomy surgery; laser retinal treatment anterior to the vortex vein ampullae; or local retinal cryotherapy, involving less than 2 quadrants, for retinal holes anterior to the vortex vein ampullae); eyes with proliferative or severe nonproliferative retinopathy; eyes with field loss attributed to a nonglaucoma condition; and eyes with dilated pupil diameter of less than 2 mm.

Eyes with *ocular hypertension* had untreated eye pressures of 24 mm Hg or more and had no evidence of glaucomatous ONH changes or visual field changes as defined above.<sup>110</sup>

Normal volunteers were recruited through e-mails and flyers at the Massachusetts General Hospital and the Massachusetts Eye and Ear Infirmary. Inclusion criteria for *normal volunteers* were as follows: refractive errors from  $-5.0$  diopters of myopia to  $+5.0$  diopters of hyperopia. Any subjects with any ocular or retinal disease other than these refractive errors were excluded. Subjects unable to be safely dilated were also excluded.

All patients were dilated prior to scanning with the Massachusetts Eye and Ear Infirmary pharmacy dilating drop combination: tropicamide 0.8% and phenylephrine 5%.<sup>111,112</sup> Artificial tears were used as needed in cases where corneal dryness may potentially affect scan quality.<sup>113-115</sup>

Spectral domain OCT scan protocol for ONH imaging was as follows: The spectral domain OCT instrument acquired 3D volume images by raster scanning a  $7 \times 7$ -mm<sup>2</sup> area centered on the ONH. Acquisition speed was 29,000 depth profiles per second, 500 depth profiles per cross-sectional image. The 3D volume images consisted of 360 cross-sectional images, acquired in 6.2 seconds. Blinking would lead to temporary loss of data, but the eye tracker tolerated short interruptions of the feedback signal without losing lock. At least 3 data sets were acquired per patient per imaging session.

Spectral domain OCT RNFL thickness maps were generated using the above information as follows: We developed a Matlab code to calculate RNFL thickness in normal and glaucoma patients. Our current code analyzed the RNFL in each cross-sectional spectral domain OCT image separately. The automated method used statistical analysis of the images to control input parameters to the edge-preserving filter and snakes algorithm. This method, which is described in more detail elsewhere, allows automated determination of the RNFL borders.<sup>80</sup> The anterior border is the vitreous/RNFL interface, and the posterior border is the RNFL/ganglion cell layer and inner plexiform layer interface. Retinal thickness maps can be generated in a similar fashion except that the posterior border is defined by the RPE.

### **SPECTRAL DOMAIN OCT REFERENCE PLANE DETERMINATION PROTOCOL**

For this subprotocol of quantitative analysis of spectral domain OCT data, all patients were recruited from the Massachusetts Eye and Ear Infirmary Glaucoma Service. Consecutive patients who were willing to participate in the study from June 2006 to November 2007 and who met the above study criteria were recruited. Only patients who were imaged with the SLD spectral domain OCT system were included.

In this pilot study of spectral domain OCT cup-disc ratio assessment utilizing an OCT reference plane, both normal and glaucomatous ONHs were imaged in order to ideally get cup-disc ratios over the whole range from 0.1 to 0.9. Patients were, however, excluded if they had cup-disc ratios of 0.1 or 0.9. Patients with no discernible cups or cup-disc ratios of 0.1 on disc photography were excluded, because these patients would presumably either not have a cup to evaluate in spectral domain OCT images or not have a cup deep enough to intersect with the reference plane for automated OCT cup-disc ratio determination. Patients with no neuroretinal rim on disc photography (ie, 0.9 cup-disc ratios) were also excluded, since the cup wall would be almost vertical and would less likely provide a specific reference plane level that would best correlate with disc photography cup-disc ratios. Patients were also excluded from this subprotocol if they had poor-quality scans due to poor signal strength, had incomplete imaging where part of the ONH was not captured in the scan, or had unusable scan data due to problems with setting up the tracker system in the machine.

For all eligible patients, disc photos were masked for patient name and clinical data. All disc photos were independently assessed by 5 glaucoma specialists for vertical cup-disc ratios.

For spectral domain OCT image processing, the vertical cup-disc ratio was automatically calculated using the standard OCT reference plane of 150  $\mu\text{m}$  above the RPE. In spectral domain OCT scans, the "cup border" was defined as the circular ring where the reference plane, which is parallel to the RPE, intersected the ONH surface. In spectral domain OCT scans, the disc border was defined by the edge of the RPE. To determine the RPE disc border at the level of the "cup border," a line perpendicular to the plane of the RPE was extended vertically to the level of the "cup border." The intersection of this line with the 150- $\mu\text{m}$  reference plane was used for "disc border" calculations. The spectral domain OCT vertical cup-disc ratio (ie, the "cup border" diameter divided by the "disc border" diameter) was determined at the midsection of the disc where the disc diameter was the greatest.

Then, for each eligible study patient, the level of the reference plane was determined for where the spectral domain OCT vertical cup-disc ratio calculation yielded a vertical cup-disc ratio value most similar to the average cup-disc ratio assessment by the 5 masked glaucoma specialists.

### **SPECTRAL DOMAIN OCT MINIMUM DISTANCE BAND CORRELATION WITH CLINICAL DATA**

Of the patients eligible for the "reference plane determination subprotocol," the first 16 eyes were randomly selected for this MDB neuroretinal rim protocol, which also utilized the SLD light source. Calculation of the MDB for all study patients will be possible in the future if this MDB calculation were fully automated. Sixteen eyes were selected for this pilot study in order to initially determine if the MDB was a clinically relevant parameter for which writing an automated algorithm might be justified in the future.

Independent of RNFL thickness calculations, the neuroretinal rim MDB can be determined as described in previous

publications.<sup>86,105</sup> The outer ring of the MDB is delimited by the ONH disc boundary, and the inner ring of the MDB is delimited by the ring of points that rest on the ONH surface and that have the shortest distance from the outer ring to the ONH surface. The ONH disc boundary was determined as the average depth of 2 boundaries—the RPE boundary and the boundary between the inner and outer segments of the photoreceptors (BIOSP). The anterior edge of the BIOSP is often easier to find because it has one of the steepest intensity gradients in the retina below the anterior boundary of the RNFL. Since the 2 boundaries should intersect each other at the ONH disc, the ONH disc boundary can easily be determined in spectral domain OCT images.

For all study patients in the MDB correlation subprotocol, all disc photos were again masked for patient name and clinical data. Five glaucoma specialists independently determined the vertical cup-disc ratios from these disc photos.

## RESULTS

Figures 3 through 16 illustrate the classic structural changes of the ONH and RNFL that are known to occur in glaucoma. Age-matched normals are used in these figures (Figures 4, 10, 11, and 12) when applicable.

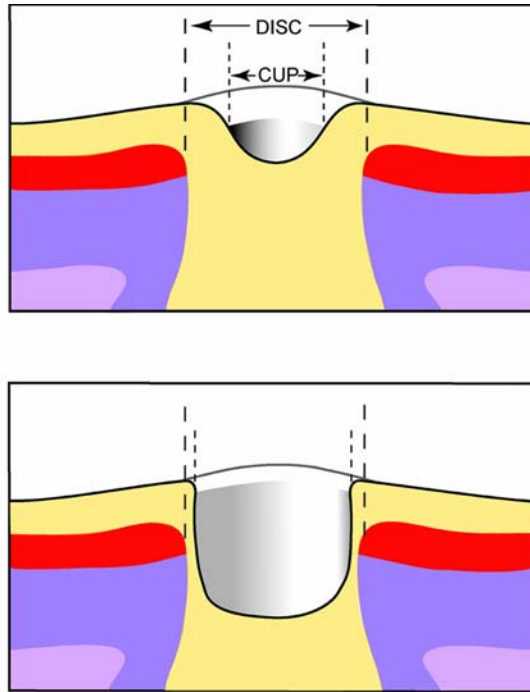


**FIGURE 3**

Schematic of glaucomatous cupping and neuroretinal rim thinning. The upper frame shows a normal optic nerve head with a small cup. The wide normal neuroretinal rim is the area outside the cup but within the disc borders. The lower frame shows glaucomatous cupping with associated thinning of the neuroretinal rim. The thinned neuroretinal rim is the small area delimited by the dotted lines, which represent the cup and disc borders. Similar cross-sectional views of the optic nerve head can be seen in spectral domain optical coherence tomography images in this thesis.

Of the normal eyes recruited for the study, normal volunteers A and B were selected as best age-matched normals for comparison with select glaucoma eyes that best showed certain glaucomatous RNFL changes. Best age-matched normals are important, because the RNFL normally thins with aging. Normal volunteer A is a 49-year-old white woman whose left eye was imaged (Figures 4 and 10). The left eye's best corrected visual acuity was 20/20 with  $+1.00 - 0.50 \times 173^\circ$  correction. She declined imaging of her dominant right eye. Normal volunteer B is a 43-year-old white man who agreed to imaging of his right eye only (Figures 11 and 12). Best corrected visual acuity was 20/20 with  $-1.25 - 0.50 \times 106^\circ$  correction.

Select glaucoma eyes are shown, since they best illustrate the classic structural ONH and RNFL changes known to occur in glaucoma. Each of these eyes represents different stages of glaucoma (ie, early, moderate, and late). These patients are described as follows.

Glaucoma patient A is a 54-year-old Cape Verdian man whose right eye was imaged (Figures 5, 8, and 15). The right eye was 20/40 best corrected with a  $-2.75 - 0.75 \times 140^\circ$  lens. Intraocular pressure was 20 mm Hg in the right eye with the patient on the following regimen: dorzolamide hydrochloride/timolol maleate twice daily, brimonidine 0.2% twice daily, pilocarpine hydrochloride 4.0% 4 times daily, and latanoprost 0.005% every night. A cup-disc ratio of 0.9 was associated with a  $10^\circ$  radius central island. The diagnosis was consistent with medically uncontrolled end-stage open-angle glaucoma.

Glaucoma patient B is a 73-year-old white woman whose left eye was imaged (Figures 6, 14, and 15). The left eye was 20/25 best corrected with a +2.25 – 1.75×86° lens. Decreased vision was consistent with a mild nuclear sclerotic cataract. Intraocular pressure was 13 mm Hg in the left eye with the patient on the following regimen: timolol maleate ophthalmic gel-forming solution (GFS) 0.5% once daily, brimonidine 0.15% twice daily, brinzolamide 1% twice daily, and latanoprost 0.005% every night. The cup-disc ratio was 0.6 OS with no neuroretinal rim inferiorly. Humphrey visual field testing revealed a dense superior paracentral scotoma. The diagnosis was consistent with moderate normal-tension glaucoma.

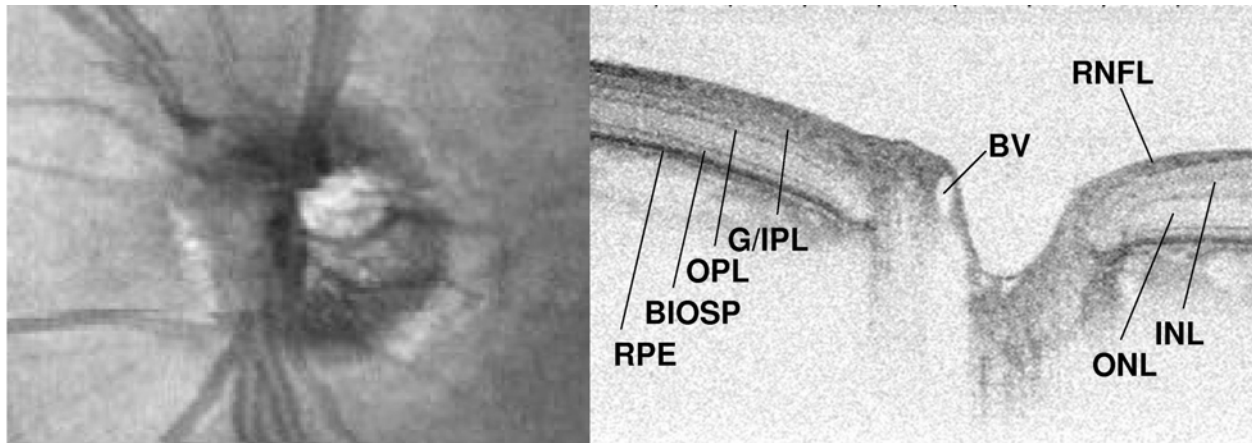


**FIGURE 4**

Spectral domain optical coherence tomography images of a normal optic nerve head with a thick neuroretinal rim. These are images of the optic nerve head of the left eye of a 49-year-old Caucasian woman (normal volunteer A). The left image is an integrated reflectance image of the optic nerve head. The right image is a horizontal cross-sectional view through the midsection of the optic nerve head. A thick normal neuroretinal rim is seen and is the tissue outside the cup border but within the disc border, which is defined by the end of the retinal pigment epithelium (RPE). To better visualize the distinct retinal layers, the image on the right is elongated vertically by a factor of 2.5. The image size shown on the right is  $5.1 \times 1.4$  mm<sup>2</sup>. The source is a titanium:sapphire laser. BIOSP, boundary between the inner and outer segments of the photoreceptors; BV, blood vessel; G/IPL, ganglion cell/inner plexiform layer; INL, inner nuclear layer; ONL, outer nuclear layer; OPL, outer plexiform layer; RNFL, retinal nerve fiber layer..

Glaucoma patient C is a 52-year-old white man whose left eye was imaged (Figure 9). The left eye was 20/40 best corrected with a -3.25 – 4.75 × 2° lens. Decreased vision was consistent with a mild nuclear sclerotic cataract. Intraocular pressure was 14 mm Hg in the left eye with use of travoprost 0.004% every night and was associated with a 0.7 cup-disc ratio. Thinning of the superior neuroretinal rim was consistent with an early inferior nasal step. The diagnosis was consistent with early primary open-angle glaucoma.

Glaucoma patient D is an 80-year-old Hispanic woman whose right eye was imaged (Figure 16, upper row). The right eye was 20/25 best corrected with a -1.00 lens. Intraocular pressure was 15 mm Hg in the right eye with the patient on the following regimen: timolol maleate GFS 0.5% once daily, pilocarpine 1% 4 times daily, and bimatoprost 0.03% every night. The cup-disc ratio was 0.8 with thinning of the superior neuroretinal rim. Humphrey visual field testing revealed an inferior arcuate defect consistent with moderate open-angle glaucoma.

Classic ONH structural changes that occur in glaucoma will be shown: glaucomatous cupping, “beanpot” cupping, bayoneting of blood vessels, and barring of circumlinear blood vessels. Classic RNFL structural changes that occur in glaucoma will also be shown: exposure of second-order blood vessels above the surface of the RNFL, RNFL thinning, and arcuate pattern of RNFL/retinal thinning. All of these structural changes will be described in more detail, going sequentially from Figures 3 through 16.

Glaucomatous cupping is associated with loss of neuroretinal rim tissue and an increase in the cup-disc ratio (Figure 3). Figure 4 shows the ONH of normal volunteer A. A thick neuroretinal rim is observed between the edge of the RPE and the ONH surface. A large white circle, a blood vessel, is seen at the left edge of the cup. The most highly reflective layers, the RPE and the RNFL,<sup>106</sup> are shown as the darkest black colors. Notably, the thick black line at the top, seen most clearly to the right of the optic nerve, shows the normal thickness of the RNFL, which is highly reflective. The 2 thick gray lines below the RNFL correspond to the plexiform layers. The thick black line at the bottom corresponds to the RPE. Above the RPE, there is a fine gray line that corresponds to the BIOSP. In contrast to normal volunteer A, the ONH of advanced open-angle glaucoma patient A (Figure 5) demonstrates significant cupping, with only a thin band of neuroretinal tissue between the RPE and the ONH surface. In Figure 5, the thinned neuroretinal rim is best seen on the right side of the cup, where there is notably little tissue between the right wall of the cup and the end of the RPE. The RNFL, which is usually black and normally highly reflective (Figure 4, normal volunteer A), is less reflective and barely discernible in this patient with glaucoma (Figure 5, glaucoma patient A), where significant thinning of the RNFL has occurred. The spectral domain OCT cross-sectional image in Figure 4 (normal volunteer A) shows good correlation with the healthy thick neuroretinal rim tissue seen in the fundus image on the left. The spectral domain OCT image in Figure 5 (glaucoma patient A) shows good correlation

with the significant loss of neuroretinal rim tissue seen in the disc photo and the severe constriction of visual field noted on Humphrey visual field testing.

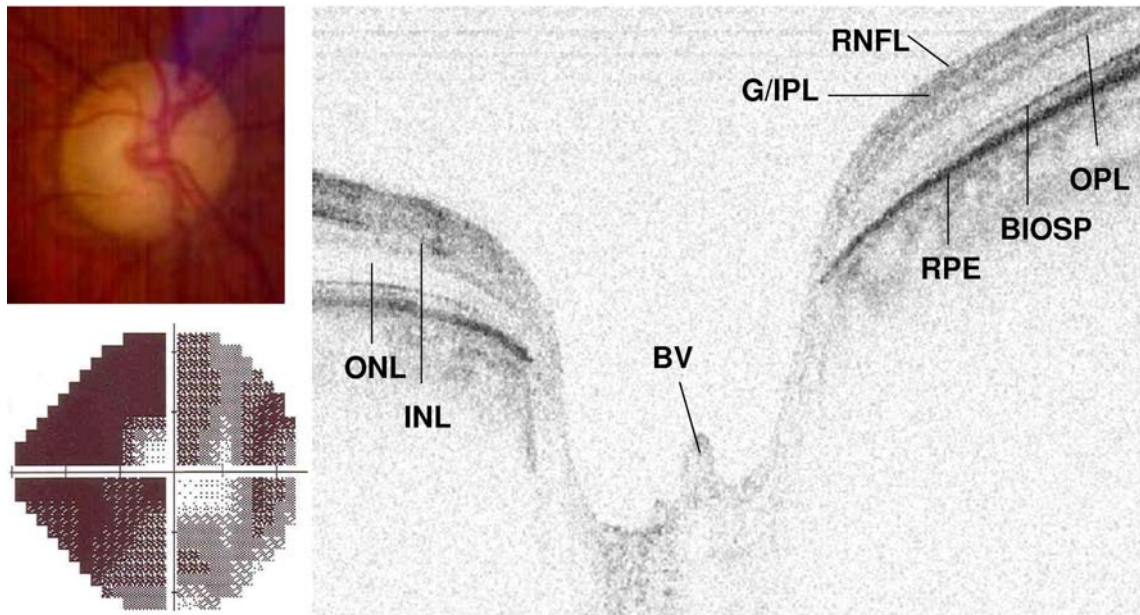


**FIGURE 5**

Spectral domain optical coherence tomography (SDOCT) image of an optic nerve head with significant glaucomatous cupping and neuroretinal rim thinning. This figure illustrates advanced glaucoma in the right eye of a 54-year-old Cape Verdian man (glaucoma patient A). The SDOCT image on the right is a horizontal cross-sectional view through the midsection of the optic nerve head. This figure demonstrates advanced glaucomatous cupping and neuroretinal rim thinning. The neuroretinal rim is seen here as a thin band of tissue between the cup border and the disc border, the latter defined by the end of the retinal pigment epithelium (RPE). The advanced changes in the SDOCT optic nerve head image correlate well with the advanced cupping seen on the disc photo and the advanced field loss on Humphrey visual field testing. To better visualize the distinct retinal layers, the SDOCT image is elongated vertically by a factor of 3.4. The image size is  $5.2 \times 1.2$  mm<sup>2</sup>. The laser source is a superluminescent diode. BIOSP, boundary between the inner and outer segments of the photoreceptors; BV, blood vessel; G/IPL, ganglion cell/inner plexiform layer; INL, inner nuclear layer; ONL, outer nuclear layer; OPL, outer plexiform layer; RNFL, retinal nerve fiber layer.

Although glaucoma patient B has only moderate normal-tension glaucoma, structural changes associated with “beanpot” cupping can be seen in her spectral domain OCT image (Figure 6). This figure is a horizontal cross section through the inferior ONH where there was no significant inferior neuroretinal rim. The classic overhanging edge that can often be seen in patients with excavation and “beanpot” cupping is demonstrated. Only the highly reflective RPE is seen as black, because the normally black and highly reflective RNFL is extremely thin and is not discernible here. Still visible are the top 2 gray layers, which are the ganglion cell/inner plexiform layer and the outer plexiform layer. Structures deep to the RPE at the left side of the cup are difficult to see because of the shadowing effect of the more superficial blood vessels.

Glaucoma classically causes RNFL thinning. Figure 7 is a schematic showing how a second-order blood vessel is normally completely buried within the thick healthy RNFL. With glaucoma, the RNFL loses its grainy surface appearance and the second-order blood vessels become exposed on the surface of the thinned RNFL. Figure 8 (left image) shows the thinned RNFL in a 54-year-old patient with advanced glaucoma (glaucoma patient A). The second-order blood vessels are shown in relief and can be seen above the surface of the thinned RNFL. Shadowing of the blood vessels is shown as the white vertical areas below the blood vessels. The image on the right in Figure 8 shows an integrated reflectance map obtained by integrating each depth profile (A-line) of the 3D spectral domain OCT scan. It is very similar to a fundus photograph or a scanning laser ophthalmoscopy image and can show the optic nerve and retinal vasculature. This integrated reflectance image has also been called an *en face* image. The 2 black horizontal lines are caused by patient blinks, and the white line indicates the position of the OCT scan in the left image. Figure 9 (glaucoma patient C) also shows a thinned RNFL in a 52-year-old patient with early open-angle glaucoma. Marked thinning of the RNFL allows for exposure of the blood vessels above the surface of the retina. As seen in normal volunteer A (Figure 10) that is age-matched (ie, within 5 years of age compared to the glaucoma eyes in Figures 8 and 9), the second-order blood vessels are normally completely buried within the RNFL. Notice the thicker black RNFL at the top of the spectral domain OCT scan. Several discontinuities due to the patient losing fixation can be noticed in the integrated reflectance map (Figure 10, right, normal volunteer A).

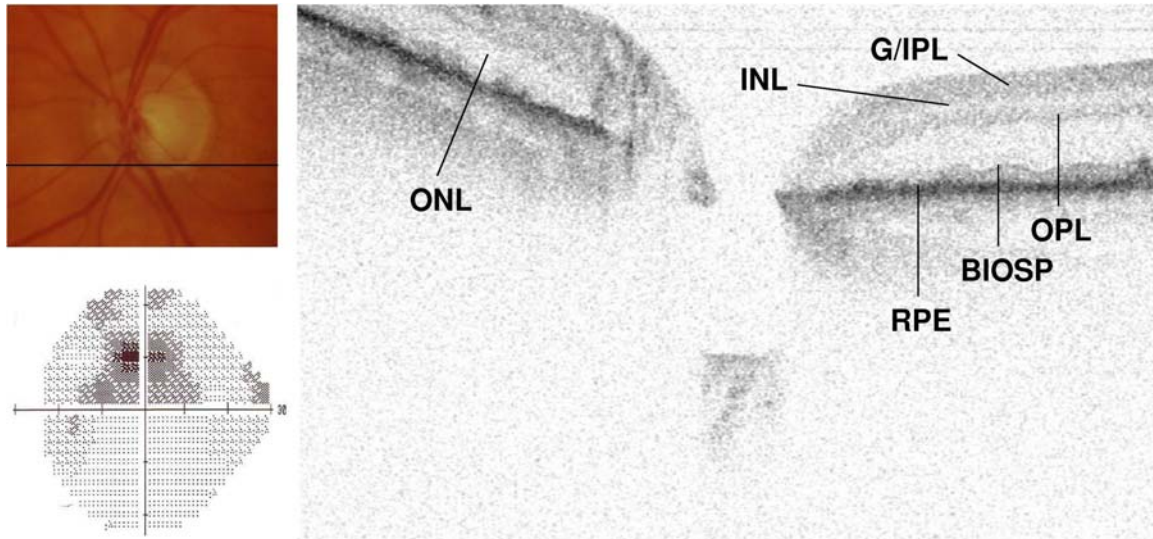


**FIGURE 6**

Spectral domain optical coherence tomography (SDOCT) image of an optic nerve head with early “beanpot” cupping in a glaucoma patient. The SDOCT image on the right shows a horizontal cross section of the inferior portion of the optic nerve head in the left eye of a 73-year-old Caucasian woman (glaucoma patient B). The SDOCT image demonstrates the overhanging edge of the neuroretinal rim, which can be seen in patients with excavation, as in glaucoma patient B, or with complete “beanpot” cupping, as in other glaucoma patients. The cup in this SDOCT image does resemble the early appearance of a “beanpot” cup shape as opposed to a cup with more vertical walls. The inferior excavation of the neuroretinal rim correlates well with the thinned inferior neuroretinal rim seen on the disc photo and the superior paracentral defect seen on visual field testing. This SDOCT image is elongated vertically by a factor of 2.85. The image size is  $5.2 \times 1.1 \text{ mm}^2$ . The source is a superluminescent diode. BIOSP, boundary between the inner and outer segments of the photoreceptors; G/IPL, ganglion cell/inner plexiform layer; INL, inner nuclear layer; ONL, outer nuclear layer; OPL, outer plexiform layer; RPE, retinal pigment epithelium.

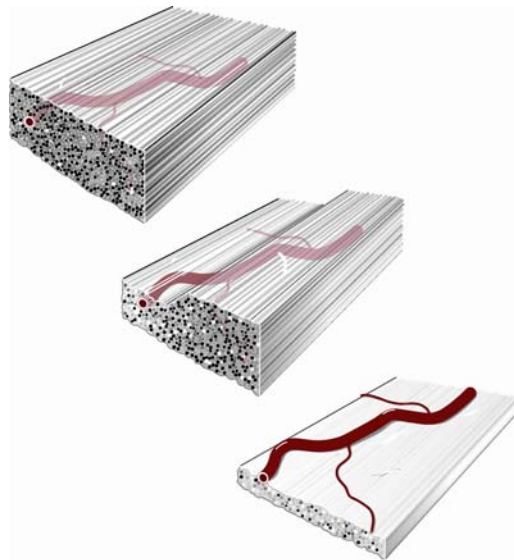


**FIGURE 7**

Schematic of the relationship between the retinal nerve fiber layer (RNFL) and the second-order blood vessels. The upper picture shows a normal thick RNFL, in which the second-order blood vessels are completely buried within the RNFL. In the middle picture, there is thinning of the left side of the RNFL layer, and the second-order blood vessel is closer to the surface here. In the lower picture, the diffusely thinned RNFL has lost its grainy surface, and the second-order blood vessels are completely exposed on the RNFL surface. Exposure of second-order blood vessels above the surface of a thinned RNFL can be seen in spectral domain optical coherence tomography images of glaucoma patients in this thesis.

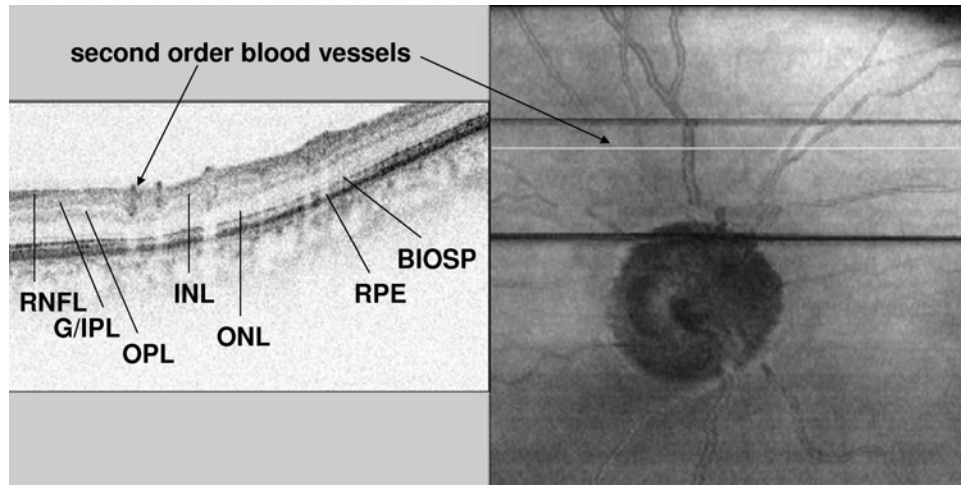


**FIGURE 8**

Spectral domain optical coherence tomography (SDOCT) image of an eye with advanced open-angle glaucoma with exposure of second-order blood vessels above a thinned retinal nerve fiber layer (RNFL) surface. Shown here is the right eye of a 54-year-old Cape Verdian man (glaucoma patient A). On the left is a horizontal cross section of the retina superior to the optic nerve head (as indicated by the white line in the right image). In the left image, the second-order blood vessels are exposed above the surface of the RNFL, which has been thinned by glaucoma. Normally, the second-order blood vessels would be completely buried within the thick RNFL. The SDOCT image on the left is elongated vertically by a factor of 3.43 and has a size of  $5.04 \times 0.94$  mm<sup>2</sup>. The image on the right is the integrated reflectance map with a size of  $5.04 \times 5.56$  mm<sup>2</sup>. This source was a superluminescent diode. BIOSP, boundary between the inner and outer segments of the photoreceptors; G/IPL, ganglion cell/inner plexiform layer; INL, inner nuclear layer; BIOSP, boundary between the inner and outer segments of the photoreceptors; ONL, outer nuclear layer; OPL, outer plexiform layer; RPE, retinal pigment epithelium.

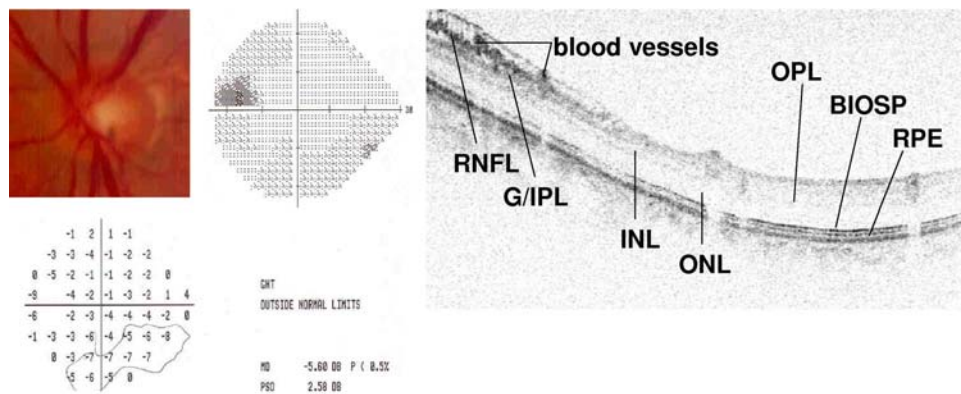


**FIGURE 9**

Spectral domain optical coherence tomography (SDOCT) image of an eye with early open-angle glaucoma with exposure of blood vessels above a thinned retinal nerve fiber layer (RNFL). The left eye of a 52-year-old patient with early open-angle glaucoma is shown (glaucoma patient C). The SDOCT image on the right is a horizontal cross section of the retina superior to the optic nerve head. Marked glaucomatous thinning of the superior RNFL is seen with exposure of the blood vessels above the surface of the retina. The normal white vertical shadowing of the blood vessels is seen all the way through the level of the retinal pigment epithelium (RPE). This thinning of the superior RNFL correlates well with an enlarged cup-disc ratio of 0.7 with thinning of the superior neuroretinal rim and with the early inferior nasal step. The SDOCT image size is  $8.1 \times 1.2$  mm<sup>2</sup> and the frame was elongated vertically by a factor of 4. The laser source was a superluminescent diode. BIOSP, boundary between the inner and outer segments of the photoreceptors; G/IPL, ganglion cell/inner plexiform layer; INL, inner nuclear layer; ONL, outer nuclear layer; OPL, outer plexiform layer.

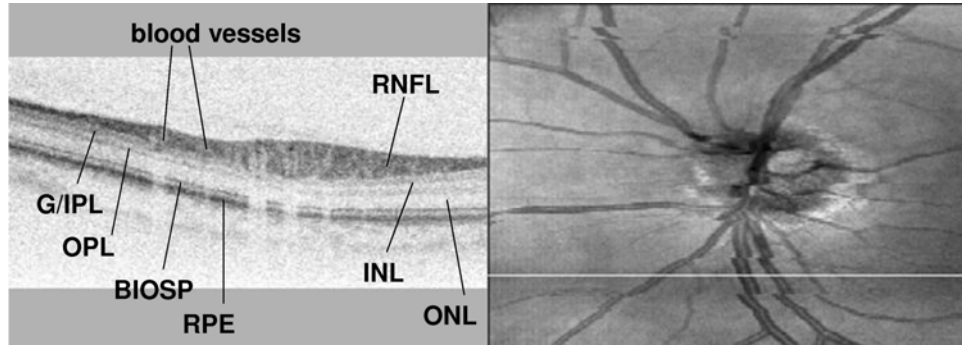


**FIGURE 10**

Spectral domain optical coherence tomography retinal nerve fiber layer (RNFL) imaging of a normal eye. The left eye of a 49-year-old Caucasian woman is imaged here (normal volunteer A). On the left is a horizontal cross section of the retina inferior to the optic nerve head (as indicated by the white line in the right image). Second-order blood vessels are completely buried within the thick black highly reflective retinal nerve fiber layer. The spectral domain optical coherence tomography image on the left is elongated vertically by a factor of 2.2 and has a size of  $5.1 \times 1.2$  mm<sup>2</sup>. The image on the right is the integrated reflectance map with a size of  $5.1 \times 5.1$  mm<sup>2</sup>. The source was a titanium:sapphire laser. BIOSP, boundary between the inner and outer segments of the photoreceptors; G/IPL, ganglion cell/inner plexiform layer; INL, inner nuclear layer; ONL, outer nuclear layer; OPL, outer plexiform layer; RPE, retinal pigment epithelium.

Other images of normal ONH and RNFL anatomy are seen in the slightly younger normal volunteer B (Figures 11 and 12). Disc photography of the right eye of normal volunteer B is correlated with a spectral domain OCT 3D volume reconstruction of the cup and the surrounding RPE (Figure 11, normal volunteer B). The vertical dimension of the 3D image is elongated for clarity of RPE surface texture and blood vessel anatomy. In Figure 12 of normal volunteer B, the second-order blood vessels are also completely buried within the thick healthy RNFL. The RNFL thickness map also illustrates the normal RNFL thickness pattern. That is, the superior and inferior RNFL is normally thicker than the nasal and temporal RNFL. The RNFL thickness also normally decreases as one scans further away from the ONH.

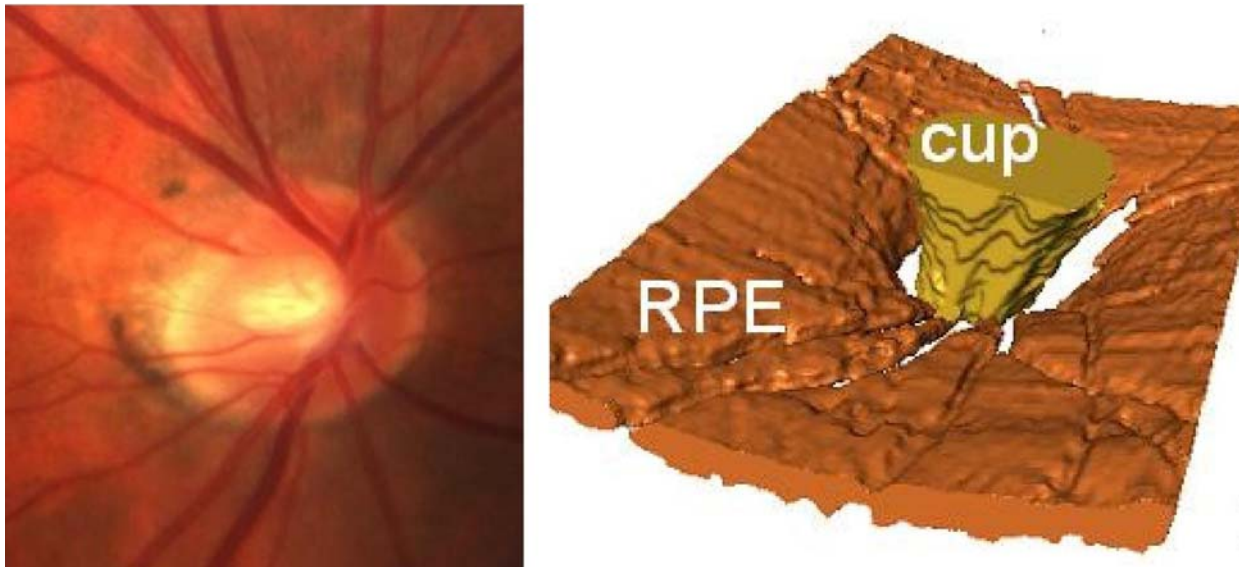


**FIGURE 11**

Spectral domain optical coherence tomography (SDOCT) image of the normal optic nerve head shown in 3-dimension (3D). The right eye of a 43-year-old Caucasian man (normal volunteer B) is imaged here. The disc photo demonstrates a healthy optic nerve head. An SDOCT image shows a 3D reconstruction of the cup and surrounding retinal pigment epithelium (RPE). The vertical dimension of the 3D image is elongated for clarity of RPE surface texture and blood vessel anatomy. The source is a titanium:sapphire laser.

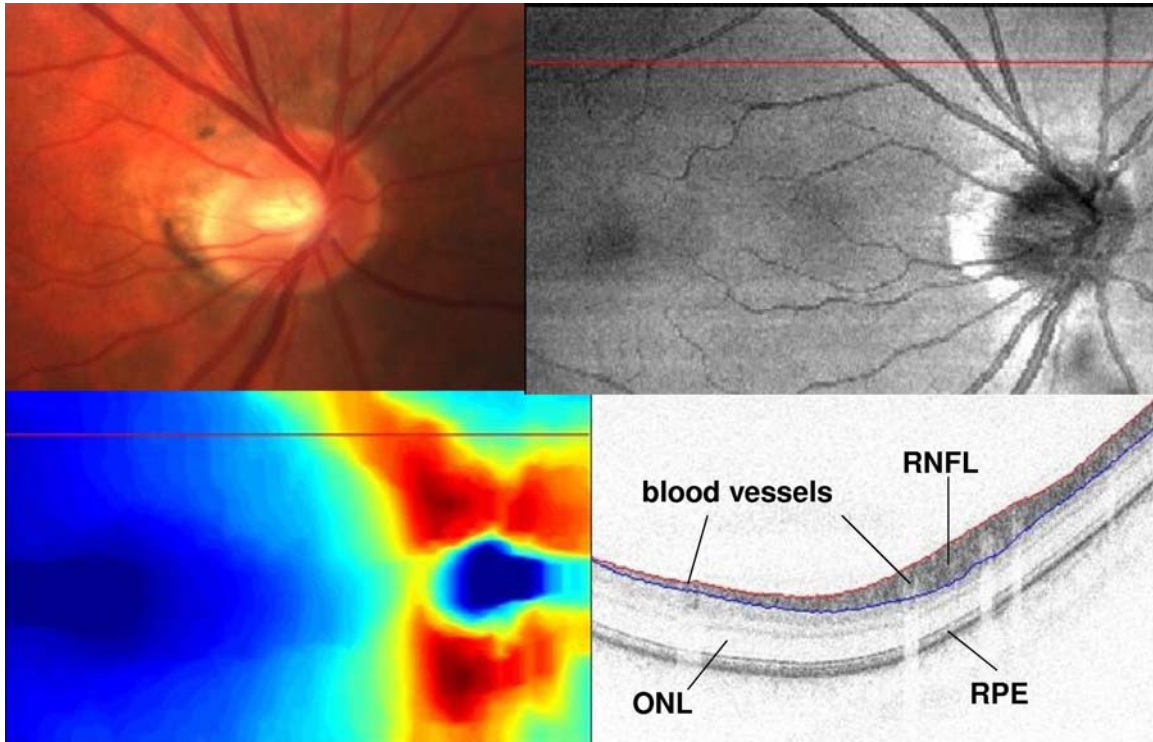


**FIGURE 12**

Example of a normal spectral domain optical coherence tomography (SDOCT) retinal nerve fiber layer (RNFL) map. The upper left image shows the disc photo of normal volunteer B. The upper right shows the integrated reflectance map. The corresponding RNFL thickness map is shown on the lower left. This RNFL thickness map displays normal anatomy, since the RNFL shows a bow-tie pattern with a thicker superior and inferior RNFL layer. The lower right shows the retinal cross-section image, with the boundaries of the RNFL outlined in red and blue. This retinal cross section also displays normal anatomy, because the second-order blood vessels are completely buried within the thick and highly reflective RNFL tissue. The size of the lower left map is  $8.81 \times 5.73 \text{ mm}^2$  and of the cross-sectional scan is  $8.81 \times 1.2 \text{ mm}^2$  (elongated vertically by a factor of 4.65). The SDOCT image (lower right) is one select frame from a 3-dimensional video consisting of 170 cross-sectional scans acquired at a rate of 29 frames per second. The red lines on the upper right and lower left images indicate the position of the SDOCT scan on the lower right. The RNFL thickness map is color scaled in microns, the darkest red indicating about  $177 \mu\text{m}$  thickness, while the darkest blue means no thickness. The source is a titanium:sapphire laser. ONL, outer nuclear layer; RPE, retinal pigment epithelium.

As the ONH neuroretinal rim undergoes progressive thinning and then excavation (Figure 13), the ONH blood vessel may demonstrate bayoneting or a double angulation as it courses along the floor of the cup and then continues along the surface of the retina (Figure 13, third frame, see inferior blood vessel). In Figure 14 (glaucoma patient B), horizontal linear scans through the ONH demonstrate bayoneting of a blood vessel along the inferior wall of the cup. From top to bottom, these horizontal cross-sectional scans show progressively more inferior scans through the ONH. Bayoneting, or double angulation, of a blood vessel occurs as it courses along the cup floor, angles around the cup rim, and then angles again to continue its course along the retinal surface. Note that the RNFL is so thin as to be barely discernible. This is consistent with the thinning of the inferior neuroretinal rim on the disc photo and the superior visual field defect seen on Humphrey visual field testing (Figure 6, glaucoma patient B).

As the ONH neuroretinal rim thins (Figure 13, third frame, see level of the black horizontal line), there may be a space between the cup wall and the circumferential blood vessel. Normally, the circumferential blood vessel hugs the cup wall (Figure 13, first and second frame). Figure 15 (glaucoma patients A and B) shows many examples of baring of the circumferential ONH blood vessels in glaucoma patients. In all these scans, there is a space between the cup wall and circumferential blood vessel. This is in contrast to the ONH blood vessel seen in a normal eye (Figure 4, normal volunteer A).

Figure 16 (upper row) shows glaucoma patient D with classic changes of the ONH and visual field with a corresponding RNFL thickness map. In Figure 16 (upper row, first column), superior neuroretinal rim thinning of the ONH is seen. This correlates with functional testing (ie, Humphrey visual field testing) and the classic inferior arcuate scotoma (Figure 16, upper row, second column). These changes of the ONH and the visual field correlate with thinning of the superior RNFL bundle in the RNFL thickness map (upper row, fourth column). This is consistent with known glaucomatous pathophysiology, which preferentially causes thinning of either the superior or inferior RNFL prior to nasal or temporal RNFL thinning.

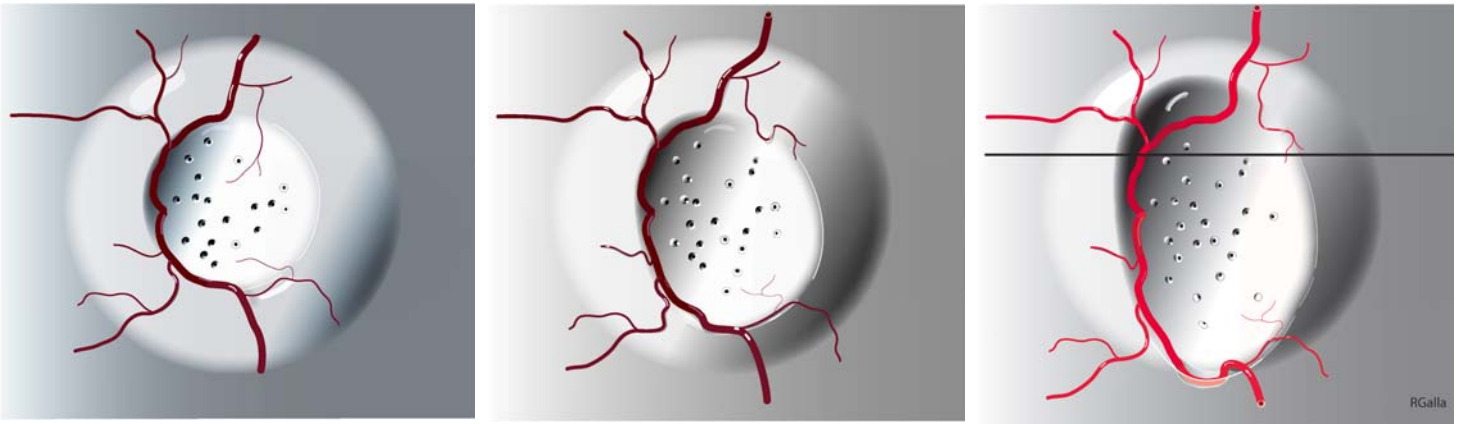


FIGURE 13

Schematic of baring of the circumferential blood vessels and bayoneting of the optic nerve head (ONH) blood vessels. This illustrates classic glaucomatous changes that occur in the ONH and its associated blood vessels. Left, a normal ONH, where the circumferential blood vessels touch the cup wall. Middle, progressive thinning of the inferior neuroretinal rim tissue, but the circumferential blood vessels still hug the cup wall. Right, a thinned superior neuroretinal rim. In this figure, there is baring of the superior circumferential blood vessels, since the superior circumferential blood vessel is no longer touching the cup wall (see level of horizontal line). Also, there is a space between the superior circumferential blood vessel and the cup wall. The inferior neuroretinal rim is excavated in this figure, and the inferior ONH blood vessel demonstrates bayoneting. Later spectral domain optical coherence tomography images will demonstrate both baring of the circumferential blood vessels and bayoneting.

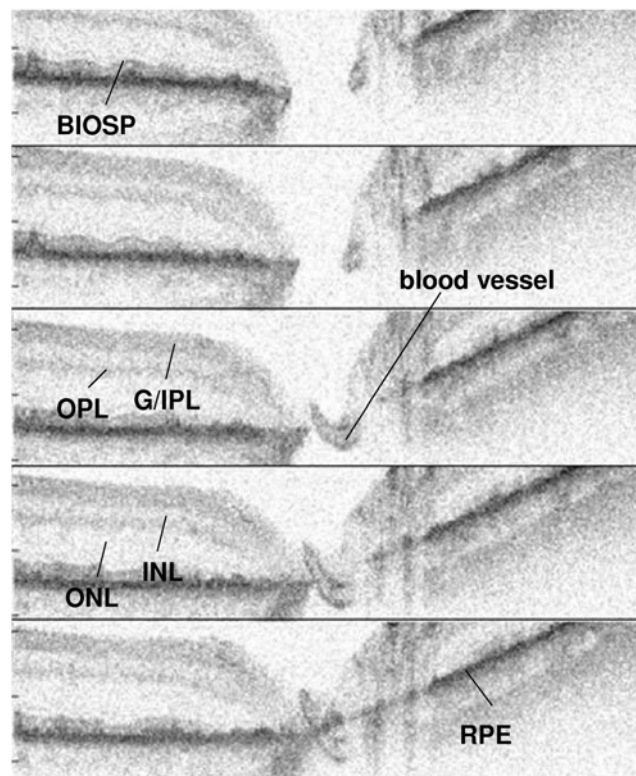
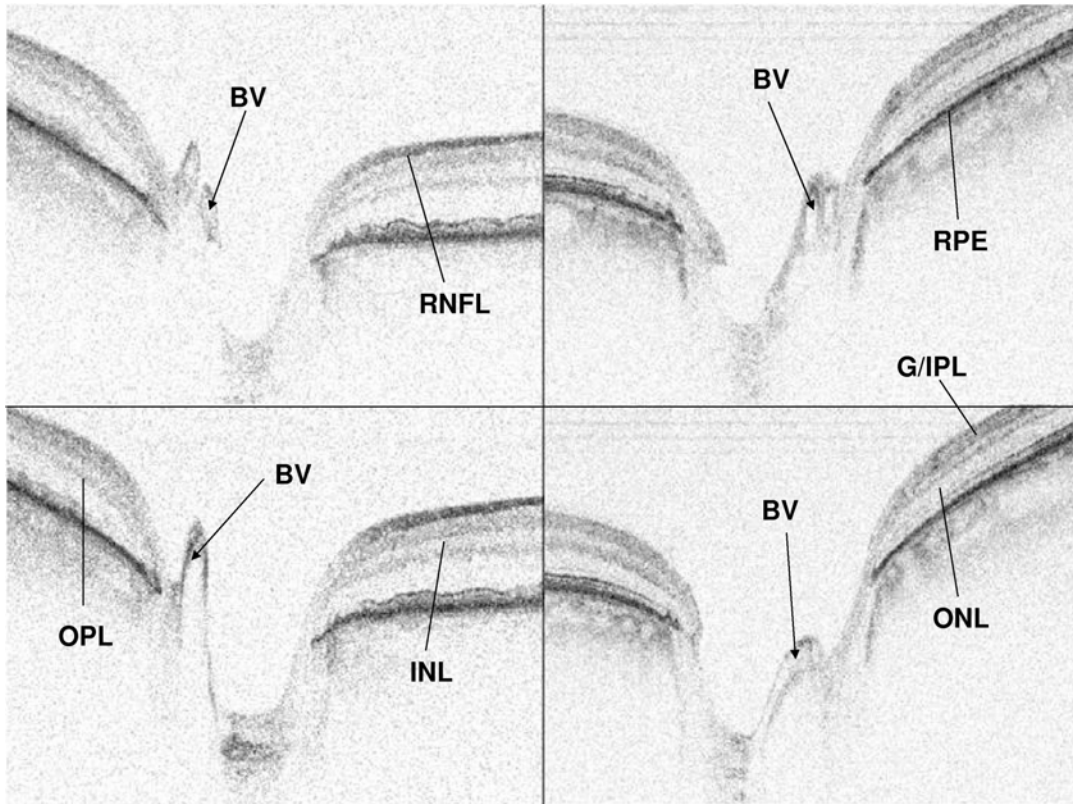


FIGURE 14

Montage of select still-images from a spectral domain optical coherence tomography video of the optic nerve head in a patient with glaucoma (glaucoma patient B) that demonstrate “bayoneting.” From the upper to lower frame, one can see bayoneting or angulation of a blood vessel as it curves along the right wall of the cup with an excavated neuroretinal rim. These images are elongated vertically by a factor of 3.56, and the size of each image is  $5.36 \times 0.41 \text{ mm}^2$ . The laser source is a superluminescent diode. BIOSP, boundary between the inner and outer segments of the photoreceptors; G/IPL, ganglion cell/inner plexiform layer; INL, inner nuclear layer; ONL, outer nuclear layer; OPL, outer plexiform layer; RPE, retinal pigment epithelium.



**FIGURE 15**

Montage of select still-images from spectral domain optical coherence tomography videos of patients with glaucoma that demonstrate baring of the circumlinear blood vessels. Baring of the circumlinear optic nerve head blood vessels is shown in these 4 frames. Baring of the circumlinear blood vessel is demonstrated by the space seen between the blood vessel and the cup wall. Prior to glaucomatous cupping or neuroretinal rim thinning, these vessels most likely touched the cup wall. Upper left, glaucoma patient B. Upper right, glaucoma patient A. Lower left, glaucoma patient B. Lower right, glaucoma patient A. These images are elongated vertically by a factor of 3.6, and their size is  $5.0 \times 1.1 \text{ mm}^2$ . The laser source is a superluminescent diode. BV, blood vessel; G/IPL, ganglion cell/inner plexiform layer; INL, inner nuclear layer; ONL, outer nuclear layer; OPL, outer plexiform layer; RNFL, retinal nerve fiber layer; RPE, retinal pigment epithelium.

Figure 16 demonstrates data from 2 open-angle glaucoma patients and introduces the concept that peripapillary retinal thickness maps may provide supplementary and useful information in the comprehensive evaluation of a glaucoma patient. In both of these cases, the classic glaucomatous arcuate pattern of nerve thinning is better seen in the retinal thickness maps (third column) than in the RNFL thickness maps (fourth column). Notably, both retinal thickness and RNFL thickness maps correlate well with disc photography neuroretinal rim thinning and visual field testing.

#### **SPECTRAL DOMAIN OCT REFERENCE PLANE DETERMINATION PROTOCOL**

For this subprotocol of quantitative analysis of spectral domain OCT data, 61 patients who met the above study inclusion criteria were recruited. After exclusion criteria were applied, 53 eyes of 33 patients were suitable for data analysis. Of the 33 patients, the average age was  $64.6 \pm 14.2$  years (range, 36-85). Of the 33 patients, 13 were men and 20 were women. Twenty were Caucasian, 5 were Hispanic, 4 were African American, 3 were Asian, and 1 was Haitian. There were 30 right eyes and 23 left eyes. Seventeen patients had normal eye examinations, except for the mild refractive errors described in the inclusion criteria. Thirteen patients had open-angle glaucoma, of which 2 had pseudoexfoliation glaucoma and 1 had normal-tension glaucoma. Three patients had ocular hypertension.

The average cup-disc ratio was  $0.5 \pm 0.2$  as determined by masked glaucoma specialist assessment of disc photography. Using the standard time domain OCT reference line of  $150 \mu\text{m}$  above the RPE, the average cup-disc ratio was  $0.5 \pm 0.2$ . Although cup-disc ratio assessments may not permit such precise evaluation, the cup-disc ratios as determined by the  $150\text{-}\mu\text{m}$  reference plane were on average 0.03 more than the cup-disc ratios as determined by disc photography assessments. The best correlation between cup-disc ratio disc photography assessments and automated spectral domain OCT cup-disc ratio determinations was with a spectral domain OCT reference plane of  $139 \mu\text{m}$  ( $\pm 98 \mu\text{m}$ ) above the RPE.

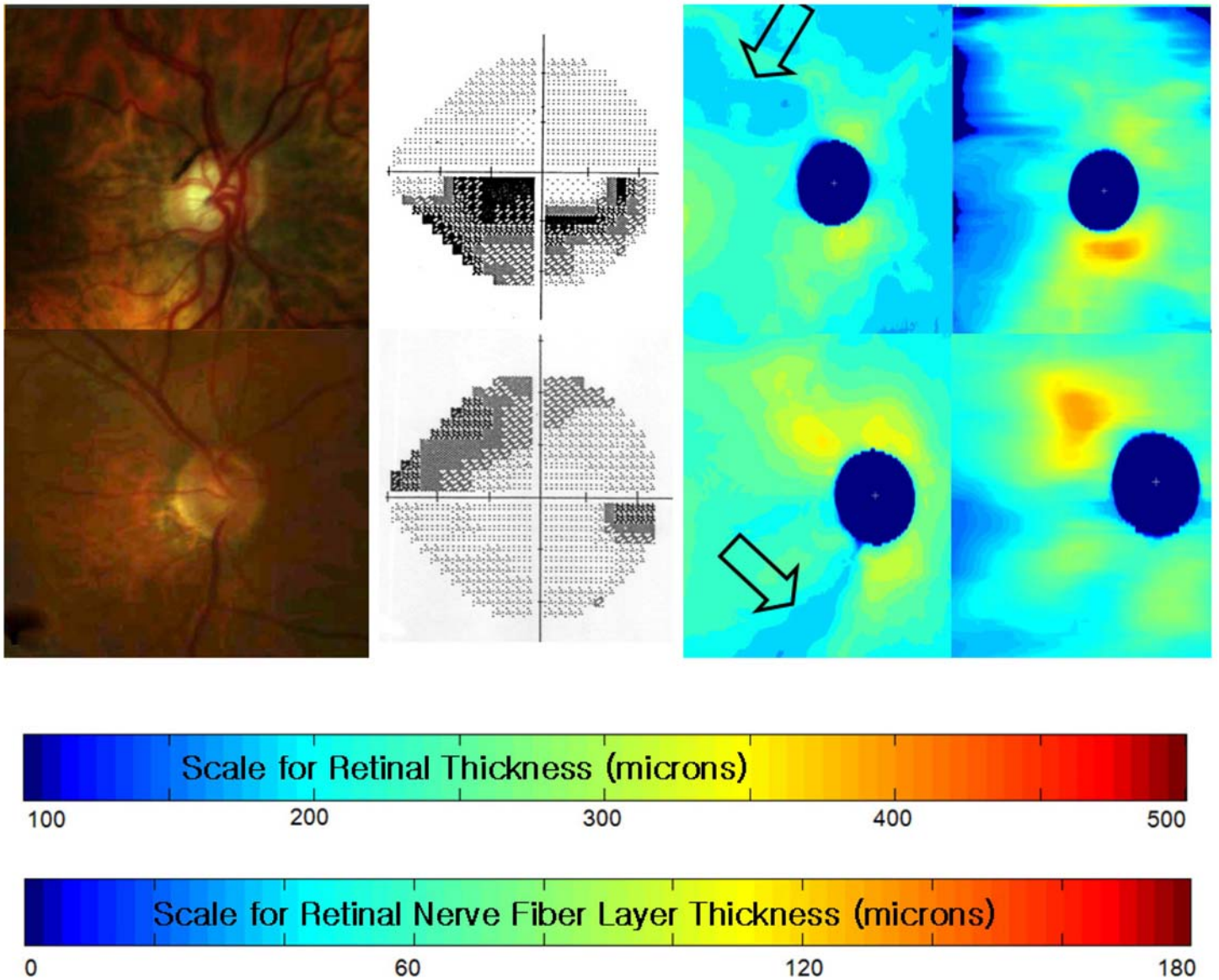


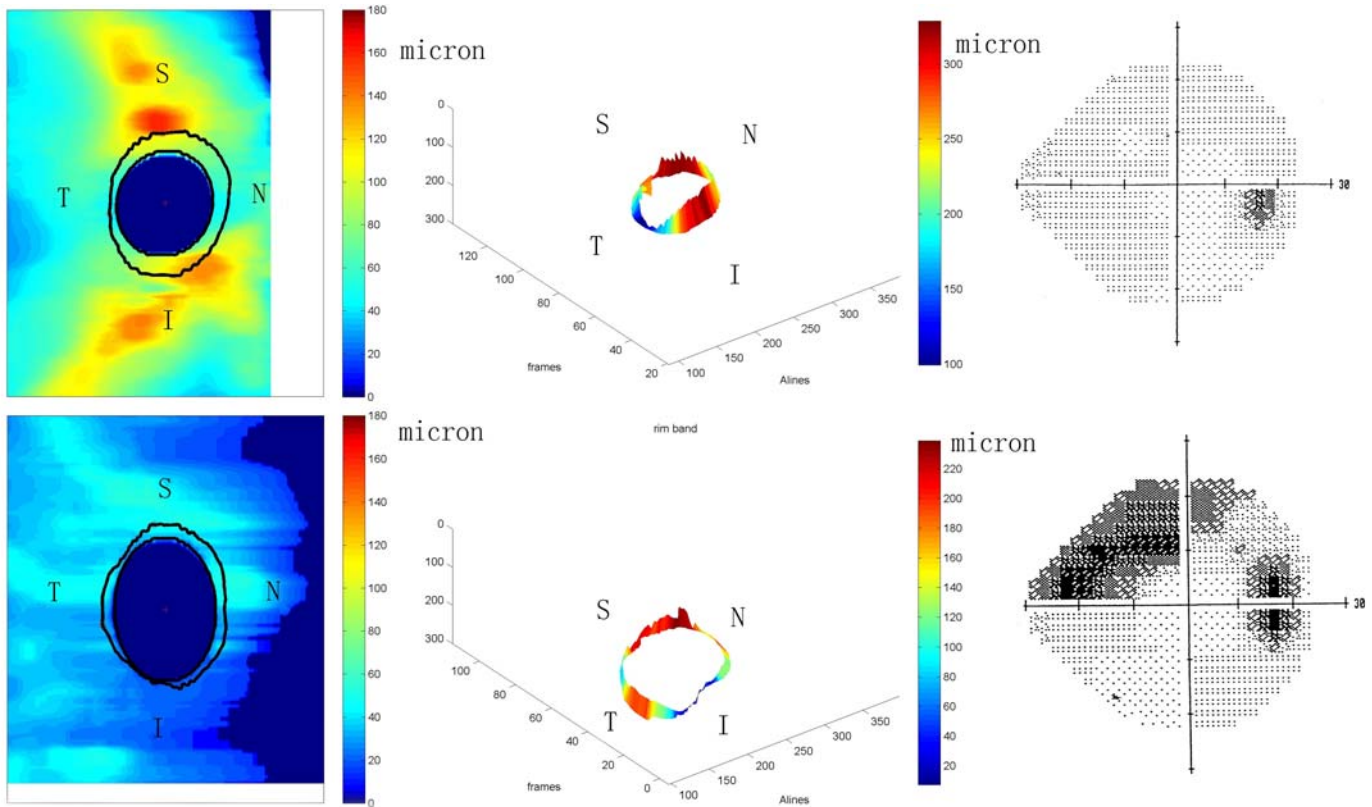
FIGURE 16

Examples of spectral domain optical coherence tomography (SDOCT) retinal thickness maps (third column) and retinal nerve fiber layer (RNFL) thickness maps (fourth column) in 2 glaucoma patients. Upper row, data is shown of the right eye of an 80-year-old Hispanic woman with primary open-angle glaucoma (glaucoma patient D). Lower row, data is shown of the left eye of an 83-year-old woman with primary open-angle glaucoma. The right eye disc photo of glaucoma patient D shows a 0.8 cup-disc ratio associated with thinning of the superior neuroretinal rim (upper, first column) and an inferior arcuate scotoma on visual field testing (upper, second column). The SDOCT retinal thickness map (upper, third column) shows a superior arcuate pattern of nerve loss, and the SDOCT RNFL thickness map (upper, fourth column) shows thinning of the superior RNFL and loss of the normal bow-tie RNFL thickness pattern. In the second glaucoma patient, cupping (lower, first column) with a superior nasal step (lower, second column) is shown. The retinal thickness map (lower, third column) shows a classic arcuate pattern of nerve loss, and the RNFL thickness map (lower, fourth column) shows that the inferior RNFL is thinner compared to the superior RNFL. The scale bars at the bottom map the retinal thickness and RNFL thickness in microns. The source is a superluminescent diode.

#### SPECTRAL DOMAIN OCT MINIMUM DISTANCE BAND CORRELATION WITH CLINICAL DATA

Of the 33 patients described above, the first 16 consecutive eyes of 13 patients that were scanned were used for MDB calculations. Four eyes of 2 patients were normal, except for the mild refractive errors described in the inclusion criteria. Ten eyes of 10 patients had open-angle glaucoma. Two eyes of 1 patient had ocular hypertension.

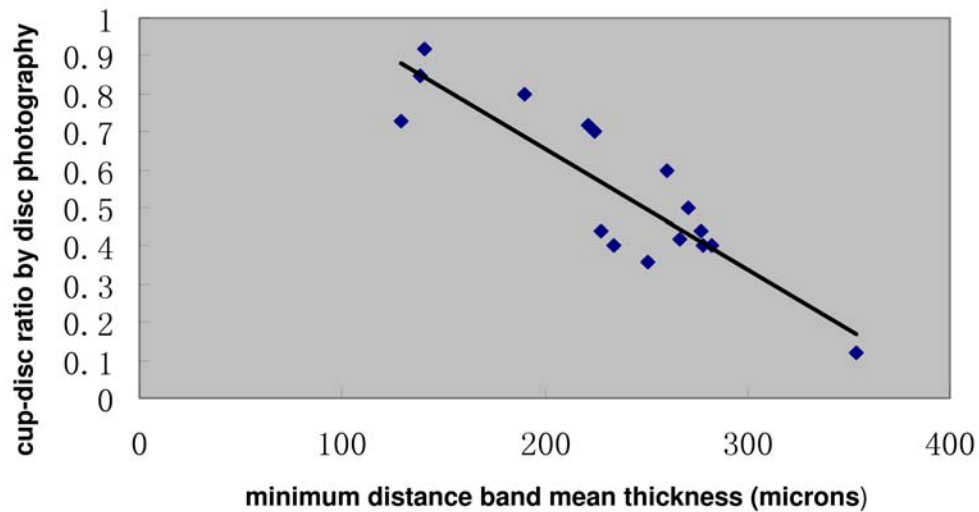
Figure 17 illustrates the MDB neuroretinal rim parameter in a normal eye (upper row) and a primary open-angle glaucoma eye (lower row). In Figure 17 (upper left, upper middle), the normal MDB neuroretinal rim rings are consistent with normal anatomy, where the superior and inferior MDB neuroretinal rim ring areas are thicker than the nasal and temporal areas of the ring. In Figure 17 (lower left, lower middle), the glaucomatous thinning of the inferior MDB neuroretinal rim ring is consistent with the superior nasal step seen on visual field testing (lower right).



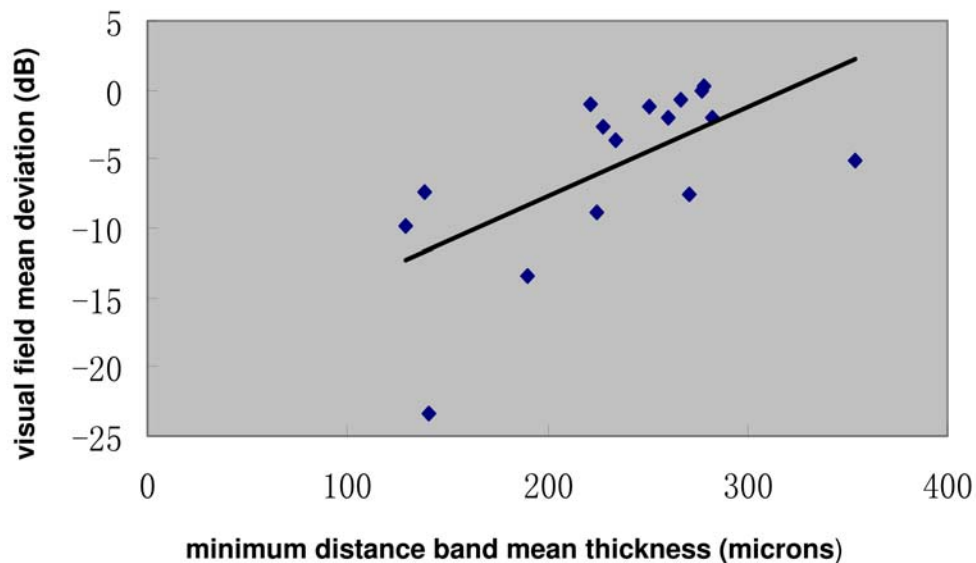
**FIGURE 17**

Correlation of minimum distance band (MDB) neuroretinal rim data with retinal nerve fiber layer (RNFL) thickness maps (first column) and Humphrey visual field testing (third column) in a normal eye (upper row) and an eye with primary open-angle glaucoma (lower row). The first column shows RNFL thickness maps generated from a spectral domain optical coherence tomography system with a superluminescent diode light source. The 2 black circles (first column) that delimit the outer and inner borders of the MDB neuroretinal rim are superimposed on the RNFL thickness maps. Three-dimensional MDBs are featured in the middle column. The thick MDB neuroretinal rim ring (upper row, first and second columns) of the normal eye correlates with the normal visual field test (upper row, third column). In contrast, thinning of the inferior MDB neuroretinal rim ring (lower row, first and second columns) of the glaucoma eye correlates with the superior nasal step on visual field testing (lower row, third column). Scale bars show the RNFL thickness in microns and the MDB mean thickness in microns. I, inferior; N, nasal; S, superior; T, temporal.

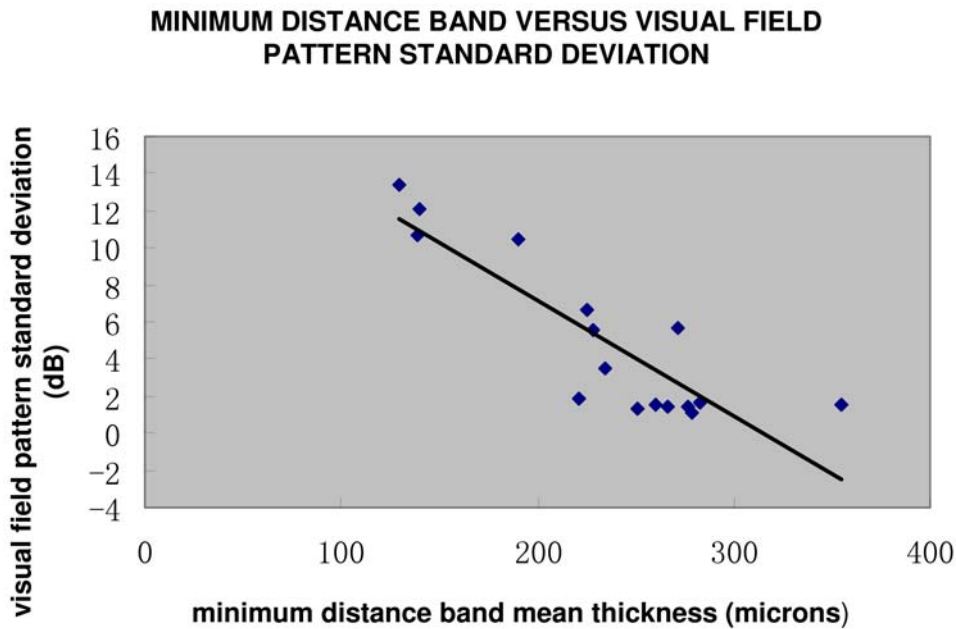
The mean thickness and area of the MDB were compared with disc photography vertical cup-disc ratio assessments and with Humphrey visual field mean deviation (MD) and pattern standard deviation (PSD). Excellent correlation was found between MDB mean thickness and all clinical parameters: cup-disc ratio assessments,  $R = -0.88$ ,  $P = .0003$ ; MD,  $R = 0.63$ ,  $P = .009$ ; PSD,  $R = -0.87$ ,  $P = .0004$ . MDB area also correlated well with all clinical parameters: cup-disc ratio assessments,  $R = -0.56$ ,  $P = .024$ ; MD,  $R = 0.63$ ,  $P = .009$ ; PSD,  $R = -0.73$ ;  $P = .001$ . MDB mean thickness and area increased as cup-disc ratio decreased, increased as visual field MD increased, and increased as visual field PSD decreased (Figures 18 through 20). In general, better correlation was found between MDB mean thickness and clinical parameters than MDB area.

**MINIMUM DISTANCE BAND VERSUS CUP-DISC RATIO****FIGURE 18**

Minimum distance band (MDB) neuroretinal rim vs vertical cup-disc ratios. This graph demonstrates that as the spectral domain optical coherence tomography MDB neuroretinal rim mean thickness in microns (x-axis) increases, the cup-disc ratio as determined by physician assessment of disc photos (y-axis) decreases. Therefore, a thicker MDB is associated with a smaller cup-disc ratio. For MDB determinations, the source is a superluminescent diode. Included are 16 eyes of 13 patients who were normal, had ocular hypertension, or had open-angle glaucoma.

**MINIMUM DISTANCE BAND VERSUS VISUAL FIELD MEAN DEVIATION****FIGURE 19**

Minimum distance band (MDB) neuroretinal rim vs visual field mean deviation. This graph demonstrates that as the spectral domain optical coherence tomography MDB neuroretinal rim mean thickness in microns (x-axis) increases, the Humphrey visual field mean deviation values in dB (y-axis) increase and normalize to zero. Therefore, a thicker MDB is associated with mean deviations closer to zero. For MDB determinations, the source is a superluminescent diode. Included are 16 eyes of 13 patients who were normal, had ocular hypertension, or had open-angle glaucoma.

**FIGURE 20**

Minimum distance band (MDB) neuroretinal rim vs visual field pattern standard deviation. This graph demonstrates that as the spectral domain optical coherence tomography MDB neuroretinal rim mean thickness in microns (x-axis) increases, the Humphrey visual field pattern standard deviation in decibels (dB; y-axis) decreases and normalizes to zero. Therefore, a thicker MDB is associated with pattern standard deviations closer to zero. For MDB determinations, the source is a superluminescent diode. Included are 16 eyes of 13 patients who were normal, had ocular hypertension, or had open-angle glaucoma.

## DISCUSSION

Video-rate spectral domain OCT allows for unprecedented simultaneous ultrahigh-speed ultrahigh-resolution ophthalmic imaging.<sup>60,76</sup> Unlike the current commercially available time domain Stratus OCT instrument and unlike ultrahigh-resolution time domain OCT, spectral domain OCT's ultrahigh acquisition speeds allow for 2D imaging in 1/29th of a second<sup>76,77</sup> as well as 3D video imaging of large areas of the posterior pole. Spectral domain OCT's ultrahigh resolutions may allow for axial resolutions of 2  $\mu\text{m}$  in the eye.<sup>60-63</sup> Compared to the leading time domain Stratus OCT machine with axial resolutions of 10  $\mu\text{m}$ , commercially available spectral domain OCT instruments generally afford axial resolutions ranging from 4 to 7  $\mu\text{m}$ . Some of these FDA-approved commercially available spectral domain OCT machines became available at the end of year 2006 and include the following: RTVue (Optovue Inc, Fremont, California), Cirrus HD-OCT (Carl Zeiss Meditec Inc, Dublin, California), Spectralis (Heidelberg Engineering Inc, Heidelberg, Germany), SOCT Copernicus (Optopol Technology, Zawiercie, Poland), and 3D OCT-1000 (Topcon, Paramus, New Jersey).

Although spectral domain OCT technology may use the same light source as time domain OCT technology (ie, either an SLD or Ti:sapphire laser source), the main difference between time domain OCT and spectral domain OCT is the way the information is processed as light comes back from the mirror in the reference arm and the eye in the sample arm (Figures 1 and 2). In contrast to time domain OCT, which utilizes a point detector or photodetector in the detector arm (Figure 1), spectral domain OCT utilizes a spectrometer, which is composed of a transmission grating and an air-spaced focusing lens (Figure 2). With spectral domain OCT, depth information is acquired by analyzing the interference patterns in a spectrum of mixed reflected lights.<sup>75,86,116-118</sup> This information from the spectrometer undergoes Fourier transformation in order to create an image. Therefore, this technology has also been referred to as Fourier domain OCT.<sup>60</sup>

Unlike time domain OCT, which achieves ultrahigh-resolution images by increasing acquisition times,<sup>72</sup> spectral domain OCT can achieve ultrahigh-resolution imaging near 2  $\mu\text{m}$  axial resolution without a significant increase in acquisition times and with a Ti:sapphire laser source.<sup>62,63,86</sup> The FDA-approved commercially available spectral domain OCT machines generally give axial resolutions of about 4 to 7  $\mu\text{m}$ , because these machines use the cheaper, easier-to-maintain SLD light source,<sup>86</sup> which may cost 10 times less than higher-resolution Ti:sapphire laser sources.

The image quality or the signal-to-noise ratio (SNR) of the spectral domain OCT systems is better than time domain OCT systems.<sup>79,119</sup> For example, in the experimental spectral domain OCT system that was built at the Massachusetts Eye and Ear Infirmary, the SLD light source was centered at 840 nm with a bandwidth range of 50 nm. The axial resolution in a time domain OCT

system would increase with optical bandwidth, but its SNR is inversely proportional to an increase in optical bandwidth.<sup>61,62</sup> Since the light source bandwidth does not affect the SNR of a spectral domain OCT system, any source can be used with spectral domain OCT without compromising image quality or SNR. Unlike Ti:sapphire laser sources, ultrabroad bandwidth SLD light sources have been developed that are compact, less expensive, and low maintenance. The combination of new light sources and the spectral domain OCT technology has greatly improved ophthalmic imaging. Also, SNR can be further reduced with pulsed illumination instead of continuous-wave illumination.<sup>81,120</sup> Like stroboscopic illumination, sample motion can be frozen by using a pulsed light source.<sup>120</sup> Pulsed illumination reduces the detrimental effects of sample motion during the scanning, thereby providing a 4.4 relative SNR advantage compared to that of continuous-wave illumination.<sup>81,86</sup> As a result, clearer images with less artifacts can be acquired. Another technology improvement that allows for better image quality is adaptive optics, which compensates for optical aberrations (eg, astigmatism, coma, spherical aberration). In order for adaptive optics to correct optical aberrations, the shape of the incoming wavefront must be measured and compensated for with a deformable mirror (for example, in Figure 2, a deformable mirror can be located in the sample arm). As a result, best lateral resolution can be achieved while further improving SNR. The lateral resolution of OCT in the eye is usually poor—typically reported at no better than 15  $\mu\text{m}$ —due to a small imaging pupil (<2 mm) and the presence of ocular aberrations, but adaptive optics can improve lateral resolutions to about 3  $\mu\text{m}$ .<sup>121</sup> Adaptive optics combined with OCT can allow for 3D imaging of cellular structures such as cone photoreceptors, microvasculature, and RNFL bundles.<sup>121-125</sup>

Optic nerve head imaging is improved with spectral domain OCT. For time domain Stratus OCT ONH imaging, 6 radial 4-mm line scans centered on the ONH create an ONH image. Interpolation is used to fill in the missing information about the ONH topography between the 6 radial line scans. Also, since a 2D Stratus OCT image takes over 1 full second to scan, microsaccades and motion artifacts are introduced, necessitating realignment of the A-lines. Therefore, true ultrahigh-resolution ONH topography images (Figures 4 and 11) were not possible until spectral domain OCT technology, since spectral domain OCT's ultrahigh acquisition speeds do not necessitate realignment of A-lines.

This report shows that spectral domain OCT can image the classic structural changes of the ONH in glaucoma. Both cupping (Figure 4 with normal volunteer A vs Figure 5 with glaucoma patient A) and “beanpot” cupping (Figure 6, glaucoma patient B) can be seen. Spectral domain OCT can also image classic changes in ONH blood vessels in glaucoma patients. For example, with glaucomatous cupping and thinning of the neuroretinal rim, the blood vessels that course along the ONH may experience a double-angulation, commonly described as bayoneting. As these blood vessels course along the floor of the cup, they eventually bend in order to climb up the side wall of the cup. As the blood vessel reaches the rim of the cup, it again bends in order to continue its path along the retinal surface. This bending, or double-angulation, is more pronounced in patients with significant glaucomatous cupping (Figure 13, third frame, and Figure 14, glaucoma patient B). Similarly, the circumferential ONH blood vessels also undergo changes relative to the ONH in a patient with glaucoma. In the normal eye, the circumferential blood vessels usually course in a circumferential fashion parallel and adjacent to the wall of the cup. These blood vessels can often be buried within the neuroretinal rim tissue or cup surface (Figure 4, normal volunteer A). As glaucomatous loss of neuroretinal rim tissue occurs, these circumferential blood vessels often no longer touch the neuroretinal rim tissue, and there can then be a resulting space between the circumferential blood vessels and the cup floor or wall (Figure 13, third frame, at level of black horizontal line, and Figure 15, glaucoma patients A and B). Spectral domain OCT video and 3D imaging of the ONH is also possible (Figure 11, normal volunteer B).

Since glaucoma is a progressive disease that can often be associated with structural changes over many years, good quantitative progression analysis of the ONH is needed. Although simple assessments of ONH surface topography changes are possible with imaging technologies, ONH topography change can be accurately assessed only if true ONH topography is being imaged in the first place, which is now possible with spectral domain OCT. In addition to ONH surface topography change algorithms, numerous and varied ONH-specific imaging parameters have been used (eg, vertical and horizontal cup-disc diameter ratio, cup-disc area ratio, cup area, cup volume, mean cup depth, disc area, rim area, rim volume). Many of these ONH-specific parameters are derived from measurements relative to a reference plane (ie, 150  $\mu\text{m}$  above the RPE for time domain OCT and 50  $\mu\text{m}$  below the temporal retinal surface for HRT). Since spectral domain OCT technology gives unprecedented ultrahigh-resolution 3D images, new spectral domain OCT algorithms need to be developed for better evaluation of the ONH in glaucoma patients. These algorithms may include evaluation of new surface topography changes as well as better reference planes.

Before describing a new 3D spectral domain OCT-specific ONH parameter, classic 1-dimensional measurements of the ONH need to be verified in spectral domain OCT images. This classic 1-dimensional parameter is the standard vertical cup-disc diameter ratio assessment as determined by both physician assessment of disc photography and the imaging reference plane, from which most ONH imaging parameters are derived. An OCT reference plane is needed for vertical cup-disc ratio assessments, since our evaluation of multiple spectral domain OCT images did not reveal either a specific OCT structure that corresponds to the cup border on a stereo disc photograph or a specific slope or angle of the spectral domain OCT cup wall that correlated well with the cup border seen on a stereo disc photo (Sun W, Association for Research in Vision and Ophthalmology Meeting, 2008, Abstract). After analysis of our pilot data on 53 eyes of 33 patients, this study showed that average vertical cup-disc ratio disc photography assessments ( $0.5 \pm 0.2$ ) as determined by 5 masked glaucoma specialists were the same as average vertical cup-disc ratios ( $0.5 \pm 0.2$ ) as determined by a spectral domain reference plane 150  $\mu\text{m}$  above the RPE. Although cup-disc ratio assessments may not permit such precise evaluation, our study did note that cup-disc ratio assessments by spectral domain OCT were on average 0.03 more than cup-disc ratio assessments by disc photography. This is consistent with the time domain OCT literature which uses a 150  $\mu\text{m}$  reference plane and which also noted that cup-disc ratio assessments by time domain Stratus OCT were the same (0.00) or slightly larger (0.11) than clinical ONH examination.<sup>94-96</sup> Therefore, our study and past time domain OCT studies suggest that perhaps a reference plane lower than 150  $\mu\text{m}$  may be more consistent with cup-disc ratios determined by disc photography. Our pilot study demonstrated best correlation between

physician cup-disc ratio assessments and spectral domain OCT cup-disc ratio assessments when a  $139 \pm 98 \mu\text{m}$  reference plane was used. In keeping with the normal ONH cup slope and shape, a slightly lower OCT reference plane would be consistent with slightly smaller cup-disc ratio assessments. Best placement of a reference plane in imaging technologies is integral, since many ONH parameters (ie, cup area, cup volume) are calculated relative to this reference plane. Nevertheless, the large reference plane standard deviation of  $98 \mu\text{m}$  in our study indicates that a reference plane for imaging technology is not a perfect concept, and other methods to better evaluate the ONH in 3D are needed. One such new method is the “minimum distance band.”

Our pilot study is the first to evaluate whether the “minimum distance band”<sup>86,105</sup> would be a clinically relevant 3D spectral domain OCT ONH neuroretinal rim parameter. Because the MDB is essentially delimited by the shortest distance between the RPE outer ring and the ONH surface inner ring, this MDB parameter may provide an objective quantification of the nerve tissue in the neuroretinal rim, since all nerve axons from the photoreceptors that course through the ONH on the way to the brain must necessarily pass through this narrow MDB, which encircles the cup. Any focal regions of thinning in this band may indicate glaucomatous neuroretinal rim thinning. Before discussing the results of the pilot study, it is important to describe the type of tissue passing through the MDB. A study of rhesus monkeys showed that this region of the neuroretinal rim consists of 94% ganglion cell nerve axons and 5% astrocytes.<sup>126</sup> Thus, nerve tissue is the main structure in the MDB. Other structures, such as blood vessels, also travel through the MDB.<sup>126,127</sup>

Figure 17 shows 2 representative eyes where the MDB neuroretinal rim parameter was calculated and then correlated with both OCT and clinical data. Figure 17 shows data from a normal eye (upper row) and from a glaucomatous eye (lower row). Figure 17, upper left, shows a normal right eye’s RNFL thickness map. The micron scale bar to the right of this image confirms normal RNFL anatomy, where the superior and inferior RNFL is thicker than the nasal and temporal RNFL. The MDB is superimposed on this RNFL thickness map and is depicted by 2 black circles. The upper middle image shows the 3D MDB neuroretinal rim displayed by itself. The micron scale bar to the right of this image also confirms normal neuroretinal rim anatomy, where the neuroretinal rim is normally thicker superiorly (S) and inferiorly (I). This correlates well with a normal visual field test (upper right). Figure 17, lower left, shows a right eye with primary open-angle glaucoma. A thinned inferior RNFL is seen in the RNFL thickness map (lower left), and the 2 black rings delimiting the MDB are also seen superimposed on this RNFL thickness map (lower left). Notably, the inferior MDB (lower left) is thinned, and this is felt to correlate with a thinner inferior neuroretinal rim. The thinned inferior MDB (lower middle) correlates well with the superior nasal step on visual field testing (lower right). In theory, this MDB neuroretinal rim parameter should be easier to measure reliably in glaucoma patients compared to RNFL thickness maps. For MDB determinations, the borders of the MDB, which are delimited by the RPE and ONH surface, are always highly reflective surfaces in OCT images of both normal and glaucomatous eyes. In contrast, RNFL thickness maps are more difficult to accurately assess in glaucoma patients, since RNFL thickness measurements are more difficult to obtain with RNFL thinning. The main problem with RNFL thickness determinations in glaucoma patients is that the posterior border of the RNFL is difficult to distinguish from the underlying layers in glaucomatous eyes. In glaucoma patients, the posterior boundary of the RNFL layer is more difficult to distinguish, since RNFL reflectivity decreases with glaucoma, which causes the thinned RNFL to have a similar reflectivity as the underlying ganglion cell layer and inner plexiform layer (Figures 6, 9, 14, and 15).

In the pilot study of 16 eyes of 13 patients where MDB was determined, both MDB mean thickness and area show excellent correlation with clinical parameters such as vertical cup-disc ratio disc photography assessments, Humphrey visual field mean deviation, and pattern standard deviation. In general, MDB mean thickness showed best correlation with clinical cup-disc ratio assessments (Figure 18;  $R = -0.88$ ), Humphrey visual field mean deviation (Figure 19;  $R = 0.63$ ), and Humphrey visual field pattern standard deviation (Figure 20;  $R = -0.87$ ). In Figures 18 through 20, we see that as MDB mean thickness increases or as the neuroretinal rim thickness increases, the cup-disc ratio is smaller and the mean deviation and pattern standard deviation values are more normal. The MDB seems to be a potentially useful parameter for evaluation of the ONH in glaucoma patients. An algorithm that automates this calculation would make future studies with larger numbers of patients possible.

The 2- $\mu\text{m}$  ultrahigh-resolution imaging capability of spectral domain OCT is essential for best glaucoma imaging of the RNFL. In contrast to adaptive optics with spectral domain OCT, which allows for imaging of individual RNFL bundles and photoreceptor cones,<sup>121-125</sup> time domain OCT’s 10- $\mu\text{m}$  axial resolution capability seems inadequate for imaging the RNFL in glaucoma. For example, longitudinal evaluation of RNFL thinning in glaucoma patients requires the clinician to determine whether RNFL thinning over time is occurring at a faster rate than expected for normal aging. In a recent longitudinal study of Stratus OCT RNFL thickness measurements (Wollstein G, American Glaucoma Society Meeting, 2008, Abstract), the expected normal rate of most rapid RNFL thinning was -0.44  $\mu\text{m}$  per year. It seems that time domain OCT technology is not sufficient for longitudinal RNFL thickness evaluations, since the axial resolution is only 10  $\mu\text{m}$  and the normal test-retest variability ranges from 3.5 to 16  $\mu\text{m}$ .<sup>128,129</sup> Even studies in monkeys where glaucomatous structural changes are expedited over weeks instead of years, RNFL thickness changes of 3.77  $\mu\text{m}$  are suggested as significant.<sup>130</sup> In addition to problems with low resolution, time domain Stratus OCT RNFL thickness measurements are largely limited to RNFL thickness values along a 3.4-mm-diameter circular scan around the ONH. Not only does this not give RNFL thickness values within the circular scan or outside the circular scan, these RNFL thickness measurements are highly dependent on exact centration of the circular scan around the ONH.<sup>131,132</sup> If the 3.4-mm-diameter circular scan is shifted either horizontally or vertically, RNFL thickness measurements are significantly affected,<sup>131</sup> since it is well known that the RNFL is thicker when closer to the ONH edge. These centration issues could be eliminated with better operator technique, eye tracking technology, or faster OCT scanning.<sup>132</sup> The latter 2 issues are addressed with our experimental spectral domain OCT system with eye tracker.

Spectral domain OCT technology can image the classic structural changes of the RNFL in glaucoma patients. Thinning of the RNFL, as well as loss of the normal high RNFL reflectivity, can easily be observed in spectral domain OCT images of glaucoma eyes

(Figure 5, glaucoma patient A; Figure 6, glaucoma patient B; Figure 8, glaucoma patient A; Figure 9, glaucoma patient C; Figure 14, glaucoma patient B; Figure 15, glaucoma patients A and B). Spectral domain OCT can also image changes in blood vessels associated with RNFL thinning. Second-order blood vessels are often completely buried within the thick healthy RNFL in the normal eye (Figure 7, upper picture; Figures 10, normal volunteer A, and 12, normal volunteer B). As the surrounding RNFL thins in the glaucomatous eye, these second-order blood vessels can become exposed and are seen in relief above the retinal surface (Figure 7, lower picture; Figures 8, glaucoma patient A, and 9, glaucoma patient C).

The problems with time domain OCT RNFL thickness measurements can be largely resolved with spectral domain OCT quantitative RNFL thickness maps.<sup>80,86</sup> Because of spectral domain OCT's improved resolution and acquisition speeds, RNFL maps can be generated (Figure 16) of large regions (eg,  $8.85 \times 5.75$  mm) of the posterior pole utilizing an automated "snakes" algorithm.<sup>80</sup> With spectral domain OCT imaging of the RNFL, 3D videos can be created that are composed of 170 frames, each consisting of 1,000 A-lines.<sup>80</sup> The importance of RNFL thickness determination in the early diagnosis of glaucoma cannot be overstated: RNFL thinning may in theory be the earliest structural change clinically detectable, since RNFL thinning by red-free photography has been shown to occur as early as 6 years before visual field loss.<sup>23</sup> RNFL imaging may therefore be the best way to diagnose pre-perimetric glaucoma. RNFL thickness maps and measurements have their limitations. Unlike ONH topography images, which are easier to obtain, RNFL thickness maps are problematic in that RNFL thickness measurements are more difficult to obtain in glaucoma patients with thinner RNFLs and poorly reflective RNFLs. Because of these glaucomatous RNFL changes, the posterior boundary of the RNFL is more difficult to accurately assess.<sup>80,86</sup> Even in time domain OCT studies of the reliability of RNFL thickness measurements, RNFL thickness measurements were more variable in glaucomatous eyes than normal eyes.<sup>128</sup>

Because of the potential difficulties with RNFL thickness maps in glaucoma patients, a retinal thickness map is another scan that can be evaluated in glaucoma patients. Retinal thickness maps are easier to obtain because the anterior boundary or vitreous/retinal surface interface is always a clear boundary with sharp reflectivity changes. The posterior RPE boundary would also be easy to obtain even in end-stage glaucoma, since it would still be highly reflective. Figure 16 demonstrates 2 glaucoma patients where retinal thickness maps (third column) better show classic arcuate defects than RNFL thickness maps (fourth column). Although RNFL thickness maps (fourth column) still show good correlation with visual field defects, these 2 cases demonstrate that retinal thickness maps may be more useful in select cases. Peripapillary retinal thickness maps should be studied in a larger series of glaucoma patients, since most studies evaluating retinal thickness in glaucoma patients have focused on the retinal thickness in the macular region, where the ganglion cells are more than one cell layer thick.<sup>133,134</sup>

Although this format does not allow demonstration of spectral domain OCT videos, 3D videos of all patients in this study have been created. Therefore, more comprehensive visualization of these glaucomatous structural changes is possible through these 3D videos of the ONH and posterior pole. Our spectral domain OCT systems were able to create 3D large area ( $20^\circ \times 20^\circ$  field of view) tomographic videos of the ONH and retina in under 10 seconds.

In conclusion, our spectral domain OCT images can depict the following classic glaucomatous structural changes: ONH cupping, "beanpot" cupping, bayoneting of ONH blood vessels, barring of ONH circumferential blood vessels, focal and diffuse RNFL thinning, and exposure of second-order blood vessels above the surface of a thinned RNFL. Spectral domain OCT determination of the classic vertical cup-disc ratio using a reference plane 150  $\mu\text{m}$  above the RPE yielded similar cup-disc ratio values as those determined by masked glaucoma specialist evaluation of standard disc photography. A new spectral domain OCT reference plane of 139  $\mu\text{m}$  yielded cup-disc ratios that best correlated with physician cup-disc ratio assessments of disc photos. A potentially useful new spectral domain OCT ONH parameter, the MDB, correlated well with clinical examination (ie, physician cup-disc ratio assessment of disc photography, Humphrey visual field mean deviation, and pattern standard deviation). Spectral domain OCT quantitative RNFL and retinal thickness maps correlated well with ONH photos and visual field defects. Despite the improvements in spectral domain OCT imaging technology, structural changes of the ONH and RNFL as seen through imaging technologies should always be interpreted within the framework of a thorough clinical examination with functional testing.<sup>135,136</sup>

This pilot study shows that video-rate spectral domain OCT technology may be used for the qualitative and quantitative evaluation of glaucoma patients. Data from this study may provide the basis for larger studies that develop new quantitative spectral domain OCT-specific algorithms which can be used for the earlier diagnosis and better monitoring of glaucoma patients. Reproducibility studies of our 3D data also need to be done, because 3D volume changes may prove to be the best method to monitor glaucoma patients over time. Better spectral domain OCT progression analysis algorithms need to be developed and tested. Although study enrollment is not yet complete for the AIGS, this prospective longitudinal glaucoma imaging study involves the GDxVCC, HRT, and time domain Stratus OCT.<sup>137</sup> A larger prospective multicenter national study of spectral domain OCT imaging in glaucoma patients needs to be done in order to better assess the potential of spectral domain OCT in clinical practice.

## ACKNOWLEDGMENTS

**Funding/Support:** This research was supported in part by the National Institutes of Health (R01 EY014975), Bethesda, Maryland (Dr Chen, Dr de Boer).

**Financial Disclosures:** Three investigators have patents on the spectral domain optical coherence tomography technology: Mircea Mujat, PhD, B. Hyle Park, PhD, and Johannes F. de Boer, PhD. Nidek had supported the research of Johannes F. de Boer, PhD.

**Conformity With Author Information:** Institutional Review Board approvals were obtained from both the Massachusetts Eye and Ear Infirmary and Massachusetts General Hospital. Informed consents were obtained for all volunteers and were in accordance with the Health Insurance Portability and Accountability Act.

Other Acknowledgments: The author would like to acknowledge the contributions of the following individuals who worked in the laboratory of Johannes F. de Boer, PhD, at the Massachusetts General Hospital, Department of Dermatology, Wellman Center for Photomedicine, Harvard Medical School, Boston, Massachusetts: Diana Burnes, BS, Mircea Mujat, PhD, B. Hyle Park, PhD, and Johannes F. de Boer, PhD. Dr de Boer was responsible for the design and construction of the spectral domain optical coherence tomography instruments at the Massachusetts Eye and Ear Infirmary and the Massachusetts General Hospital. The author would also like to acknowledge past and present Massachusetts Eye and Ear Infirmary glaucoma research fellows Kayoung Yi, MD, PhD, and Huijuan Wu, MD, PhD, for their help in this research. In addition, the author would like to acknowledge the 4 other past and present Massachusetts Eye and Ear Infirmary glaucoma specialists who participated as masked evaluators of the stereo disc photos: Kayoung Yi, MD, PhD, Huijuan Wu, MD, PhD, Anupama Anchala, MD, and Andrea Jue, MD. The author is grateful for their invaluable help in the design and conduct of the study (J.D.) and the collection, management, analysis, and interpretation of the data (K.Y., D.B., M.M., H.W., B.H.P., J.D.).

## REFERENCES

1. The International Bank for Reconstruction and Development—the World Bank. In: *World Development Report*. Oxford: Oxford University Press; 1993:1-348.
2. Quigley HA. Number of people with glaucoma worldwide. *Br J Ophthalmol* 1996;80:389-393.
3. Quigley HA, Broman AT. The number of people with glaucoma worldwide in 2010 and 2020. *Br J Ophthalmol* 2006;90:262-267.
4. Quigley HA, Vitale S. Models of open-angle glaucoma prevalence and incidence in the United States. *Invest Ophthalmol Vis Sci* 1997;38:83-91.
5. Kini MM, Leibowitz HM, Colton T, et al. Prevalence of senile cataract, diabetic retinopathy, senile macular degeneration, and open-angle glaucoma in the Framingham eye study. *Am J Ophthalmol* 1978;85:28-34.
6. Friedman DS, Wolfs RC, O'Colmain BJ, et al. Prevalence of open-angle glaucoma among adults in the United States. *Arch Ophthalmol* 2004;122:532-538.
7. Sommer A, Tielsch JM, Katz J, et al. Racial differences in the cause-specific prevalence of blindness in east Baltimore. *N Engl J Med* 1991;325:1412-1417.
8. Mason RP, Kosoko O, Wilson MR, et al. National Survey of the prevalence and risk factors of glaucoma in St. Lucia, West Indies. Part I. Prevalence findings. *Ophthalmology* 1989;96:1363-1368.
9. Wallace J, Lovell HG. Glaucoma and intraocular pressure in Jamaica. *Am J Ophthalmol* 1969;67:93-100.
10. Tielsch JM, Sommer A, Katz J, et al. Racial variations in the prevalence of primary open-angle glaucoma. The Baltimore Eye Survey. *JAMA* 1991;266:369-374.
11. Leske MC, Connell AM, Wu SY, et al. Incidence of open-angle glaucoma: the Barbados Eye Studies. The Barbados Eye Studies Group. *Arch Ophthalmol* 2001;119:89-95.
12. Dielemans I, Vingerling JR, Wolfs RC, et al. The prevalence of primary open-angle glaucoma in a population-based study in the Netherlands. The Rotterdam Study. *Ophthalmology* 1994;101:1851-1855.
13. Leske MC, Connell AM, Schachat AP, et al. The Barbados Eye Study. Prevalence of open angle glaucoma. *Arch Ophthalmol* 1994;112:821-829.
14. Mitchell P, Smith W, Attebo K, et al. Prevalence of open-angle glaucoma in Australia. The Blue Mountains Eye Study. *Ophthalmology* 1996;103:1661-1669.
15. King AJ, Reddy A, Thompson JR, et al. The rates of blindness and of partial sight registration in glaucoma patients. *Eye* 2000;14:613-619.
16. Coleman AL. Glaucoma. *Lancet* 1999;354:1803-1810.
17. Quigley HA, Addicks EM, Green WR. Optic nerve damage in human glaucoma. III. Quantitative correlation of nerve fiber loss and visual field defect in glaucoma, ischemic neuropathy, papilledema, and toxic neuropathy. *Arch Ophthalmol* 1982;100:135-146.
18. Shields MB. Visual function in glaucoma. In: Shields MB, ed. *Textbook of Glaucoma*. Baltimore: Williams & Wilkins;1992:135.
19. Kerrigan-Baumrind LA, Quigley HA, Pease ME, et al. Number of ganglion cells in glaucoma eyes compared with threshold visual field tests in the same persons. *Invest Ophthalmol Vis Sci* 2000;41:741-748.
20. Reyes RD, Tomita G, Kitazawa Y. Retinal nerve fiber layer thickness within the area of apparently normal visual field in normal-tension glaucoma with hemifield defect. *J Glaucoma* 1998;7:329-335.
21. Schuman JS, Hee MR, Puliafito CA, et al. Quantification of nerve fiber layer thickness in normal and glaucomatous eyes using optical coherence tomography. *Arch Ophthalmol* 1995;113:586-596.
22. Blumenthal EZ, Weinreb RN. Assessment of the retinal nerve fiber layer in clinical trials of glaucoma neuroprotection. *Surv Ophthalmol* 2001;45(Suppl 3):S305-312; discussion S332-334.
23. Sommer A, Katz J, Quigley HA, et al. Clinically detectable nerve fiber atrophy precedes the onset of glaucomatous field loss. *Arch Ophthalmol* 1991;109:77-83.
24. Deleon-Ortega JE, Arthur SN, McGwin G, et al. Discrimination between glaucomatous and nonglaucomatous eyes using quantitative imaging devices and subjective optic nerve head assessment. *Invest Ophthalmol Vis Sci* 2006;47:3374-3380.
25. Keltner JS, Johnson CA, Anderson DR, et al. The association between glaucomatous visual fields and optic nerve head features in the Ocular Hypertension Treatment Study. *Ophthalmology* 2006;113:1603-1612.

26. Mills RP. Glaucoma imaging: technology in progress. *J Glaucoma* 1999;8:87-89.
27. Greaney MJ, Hoffman DC, Garway-Heath DF, et al. Comparison of optic nerve imaging methods to distinguish normal eyes from those with glaucoma. *Invest Ophthalmol Vis Sci* 2002;43:140-145.
28. Zangwill L, Shakiba S, Caprioli J, et al. Agreement between clinicians and a confocal scanning laser ophthalmoscope in estimating cup/disk ratios. *Am J Ophthalmol* 1995;199:415-421.
29. Varma R, Spaeth GL, Steinmann WC, et al. Agreement between clinicians and an image analyzer in estimating cup-to-disc ratios. *Arch Ophthalmol* 1989;107:526-529.
30. Varma R, Steinmann WC, Scott IU. Expert agreement in evaluating the optic disc for glaucoma. *Ophthalmology* 1992;99:215-221.
31. Tielsch JM, Katz J, Quigley HA, et al. Intraobserver and interobserver agreement in measurement of optic disc characteristics. *Ophthalmology* 1988;95:350-356.
32. Feuer WJ, Parrish RK, Schiffman JC, et al. The Ocular Hypertension Treatment Study: reproducibility of cup/disk ratio measurements over time at an optic disc reading center. *Am J Ophthalmol* 2002;133:19-28.
33. Keltner JL, Johnson CA, Quigg JM, et al. Confirmation of visual field abnormalities in the Ocular Hypertension Treatment Study. *Arch Ophthalmol* 2000;118:1187-1194.
34. Hemenger RP. Birefringence of a medium of tenuous parallel cylinders. *App Opt* 1989;28:4030-4034.
35. Zhou Q, Knighton RW. Light scattering and form birefringence of parallel cylindrical arrays that represent cellular organelles of the retinal nerve fiber layer. *Appl Opt* 1997;36:2273-2285.
36. Schuman JS, Hee MR, Puliafito CA, et al. Quantification of nerve fiber layer thickness in normal and glaucomatous eyes using optical coherence tomography. *Arch Ophthalmol* 1995;113:586-596.
37. Cense B, Chen TC, Park BH, et al. Thickness and birefringence of healthy retinal nerve fiber layer tissue measured with polarization-sensitive optical coherence tomography. *Invest Ophthalmol Vis Sci* 2004;45:2606-2612.
38. Huang XR, Bagga H, Greenfield DS, et al. Variation of peripapillary retinal nerve fiber layer birefringence in normal human subjects. *Invest Ophthalmol Vis Sci* 2004;45:3073-3080.
39. Choplin NT, Lundy DC. The sensitivity and specificity of scanning laser polarimetry in the detection of glaucoma in a clinical setting. *Ophthalmology* 2001;108:899-904.
40. Tribble JR, Schultz RO, Robinson JC, et al. Accuracy of scanning laser polarimetry in the diagnosis of glaucoma. *Arch Ophthalmol* 1999;117:1298-1304.
41. Sinai MJ, Essock EA, Fechtner RD, et al. Diffuse and localized nerve fiber layer loss measured with a scanning laser polarimeter: sensitivity and specificity of detecting glaucoma. *J Glaucoma* 2000;9:154-162.
42. Zangwill LM, Bowd C, Berry CC, et al. Discriminating between normal and glaucomatous eyes using the Heidelberg Retina Tomograph, GDx Nerve Fiber Analyzer, and Optical Coherence Tomograph. *Arch Ophthalmol* 2001;119:985-993.
43. Harizman N, Zelefsky JR, Iltchev E, Tello C, Ritch R, Liebmann JM. Detection of glaucoma using operator-dependent versus operator-independent classification in the Heidelberg retinal tomograph-III. *Br J Ophthalmol* 2006;90:1390-1392.
44. Moreno-Montanes J, Anton A, Garcia N, Mendiluce L, Ayala E, Sebastian A. Glaucoma probability score vs Moorfields classification in normal, ocular hypertensive, and glaucomatous eyes. *Am J Ophthalmol* 2008;145:360-368.
45. Ferreras A, Pablo LE, Larrosa JM, Polo V, Pajarin AB, Honrubia FM. Discriminating between normal and glaucoma-damaged eyes with the Heidelberg Retina Tomograph 3. *Ophthalmology* 2008;115:775-781.
46. Coops A, Henson DB, Kwartz AJ, Artes PH. Automated analysis of Heidelberg retina tomograph optic disc images by glaucoma probability score. *Invest Ophthalmol Vis Sci* 2006;47:5348-5355.
47. Lu AT, Wang M, Varma R, et al. Combining nerve fiber layer parameters to optimize glaucoma diagnosis with optical coherence tomography. *Ophthalmology* 2008;115:1352-1357.
48. Medeiros FA, Zangwill LM, Bowd C, et al. Evaluation of retinal nerve fiber layer, optic nerve head, and macular thickness measurements for glaucoma detection using optical coherence tomography. *Am J Ophthalmol* 2005;139:44-55.
49. Hougaard JL, Heijl A, Bengtsson B. Glaucoma detection using different Stratus optical coherence tomography protocols. *Acta Ophthalmol Scand* 2007;85:251-256.
50. Brusini P, Salvetat ML, Zeppieri M, et al. Comparison between GDxVCC scanning laser polarimetry and Stratus OCT optical coherence tomography in the diagnosis of chronic glaucoma. *Acta Ophthalmol Scand* 2006;84:650-655.
51. Wollstein G, Ishikawa H, Wang J, et al. Comparison of three optical coherence tomography scanning areas for detection of glaucomatous damage. *Am J Ophthalmol* 2005;139:39-43.
52. Chen HY, Huang ML. Discrimination between normal and glaucomatous eyes using Stratus optical coherence tomography in Taiwan Chinese subjects. *Graefes Arch Clin Exp Ophthalmol* 2005;243:894-902.
53. Pueyo V, Polo V, Larrosa JM, et al. Diagnostic ability of the Heidelberg Retina Tomograph, optical coherence tomograph, and scanning laser polarimeter in open-angle glaucoma. *J Glaucoma* 2007;16:173-177.
54. Anton A, Moreno-Montanes J, Blazquez F, et al. Use of optical coherence tomography parameters of the optic disc and retinal nerve fiber laser to differentiate glaucomatous, ocular hypertensive, and normal eyes. *J Glaucoma* 2007;16:1-8.
55. Hougaard JL, Heijl A, Bengtsson B. Glaucoma detection by Stratus OCT. *J Glaucoma* 2007;16:302-306.
56. Parikh R, Parikh S, Sekhar GC, et al. Diagnostic capability of optical coherence tomography (Stratus OCT3) in early glaucoma. *Ophthalmology* 2007;114:2238-2243.

57. Chen HY, Huang ML, Hung PT. Logistic regression analysis for glaucoma diagnosis using Stratus optical coherence tomography. *Optom Vis Sci* 2006;83:527-534.
58. Medeiros FA, Zangwill LM, Bowd C, et al. Comparison of the GDx VCC scanning laser polarimeter, HRTII confocal scanning laser ophthalmoscope, and Stratus OCT optical coherence tomograph for the detection of glaucoma. *Arch Ophthalmol* 2004;122:827-837.
59. Drexler W, Morgner U, Ghanta RK, Kartner FX, Schuman JS, Fujimoto JG. Ultrahigh-resolution ophthalmic optical coherence tomography. *Nat Med* 2001;7:502-507.
60. Chen TC, Cense B, Pierce MC, et al. Spectral domain optical coherence tomography: ultrahigh-speed, ultrahigh-resolution ophthalmic imaging. *Arch Ophthalmol* 2005;123:1715-1720.
61. Cense B, Nassif N, Chen TC, et al. Ultrahigh-resolution high-speed retinal imaging using spectral-domain optical coherence tomography. *Opt Express* 2004;12:2435-2447.
62. Wojtkowski M, Srinivasan V, Ko T, et al. Ultrahigh-resolution, high-speed, Fourier domain optical coherence tomography and methods for dispersion compensation. *Opt Express* 2004;12:2404-2422.
63. Wojtkowski M, Srinivasan V, Fujimoto JG, et al. Three-dimensional retinal imaging with high-speed ultrahigh-resolution optical coherence tomography. *Ophthalmology* 2005;112:1734-1746.
64. Sanchez-Galeana C, Bowd C, Blumenthal EZ, et al. Using optical imaging summary data to detect glaucoma. *Ophthalmology* 2001;108:1812-1818.
65. Lalezary M, Medeiros FA, Weinreb RN, et al. Baseline optical coherence tomography predicts the development of glaucomatous change in glaucoma suspects. *Am J Ophthalmol* 2006;142:576-582.
66. Zangwill LM, Weinreb RN, Beiser JA, et al. Baseline topographic optic disc measurements are associated with the development of primary open-angle glaucoma. *Arch Ophthalmol* 2005;123:1188-1197.
67. Zangwill LM, Weinreb RN, Berry CC, et al. The confocal scanning laser ophthalmoscopy ancillary study to the ocular hypertension treatment study: study design and baseline factors. *Am J Ophthalmol* 2004;137:219-227.
68. Alencar LM, Bowd C, Weinreb RN, et al. Comparison of HRT-3 glaucoma probability score and subjective stereophotograph assessment for prediction of progression in glaucoma. *Invest Ophthalmol Vis Sci* 2008;49:1898-1906.
69. Mohammadi K, Bowd C, Weinreb RN, et al. Retinal nerve fiber layer thickness measurements with scanning laser polarimetry predict glaucomatous visual field loss. *Am J Ophthalmol* 2004;138:592-601.
70. Huang D, Swanson EA, Lin CP, et al. Optical coherence tomography. *Science* 1991;254:1178-1181.
71. Drexler W, Morgner U, Kärtner FX, et al. In vivo ultrahigh-resolution optical coherence tomography. *Opt Letters* 1999;24:1221-1223.
72. Drexler W, Sattmann H, Hermann B, et al. Enhanced visualization of macular pathology with the use of ultrahigh-resolution optical coherence tomography. *Arch Ophthalmol* 2003;121:695-706.
73. Ko TH, Fujimoto JG, Duker JS, et al. Comparison of ultrahigh- and standard-resolution optical coherence tomography for imaging macular hole pathology and repair. *Ophthalmology* 2004;111:2033-2043.
74. Wollstein G, Paunescu LA, Ko TH, et al. Ultrahigh-resolution optical coherence tomography in glaucoma. *Ophthalmology* 2005;112:229-237.
75. Wojtkowski M, Leitgeb R, Kowalczyk A, et al. In vivo human retinal imaging by Fourier domain optical coherence tomography. *J Biomed Opt* 2002;7:457-463.
76. Nassif N, Cense B, Park BH, et al. In-vivo human retinal imaging by ultra high-speed spectral domain optical coherence tomography. *Opt Lett* 2004;29:480-482.
77. Nassif N, Cense B, Park BH, et al. In vivo high-resolution video-rate spectral domain optical coherence tomography of the human retina and optic nerve. *Opt Express* 2004;12:367-376.
78. White BR, Pierce M, Nassif N, et al. In vivo dynamic human retinal blood flow imaging using ultra-high-speed spectral domain optical doppler tomography. *Opt Express* 2003;11:3490-3497.
79. de Boer JF, Cense B, Park BH, et al. Improved signal-to-noise ratio in spectral-domain compared with time-domain optical coherence tomography. *Opt Lett* 2003;28:2067-2069.
80. Mujat M, Chan R, Cense B, et al. Retinal nerve fiber layer thickness map. *Opt Express* 2005;13:9480-9491.
81. You JW, Chen TC, Mujat M, et al. Pulsed illumination spectral-domain optical coherence tomography for human retinal imaging. *Opt Express* 2006;14:6739-6748.
82. Mujat M, Park BH, Cense B, et al. Autocalibration of spectral-domain optical coherence tomography spectrometers for in vivo quantitative retinal nerve fiber layer birefringence determination. *J Biomed Opt* 2007;12:1-6.
83. Maguluri G, Mujat M, Park BH, et al. Three dimensional tracking for volumetric spectral domain optical coherence tomography. *Opt Express* 2007;15:16808-16817.
84. Yi K, Mujat M, Park BH, et al. Spectral domain optical coherence tomography for quantitative evaluation of drusen and associated structural changes in non-neovascular age related macular degeneration. *Br J Ophthalmol* 2009;93:176-181.
85. Yi K, Mujat M, Sun W, et al. Imaging of optic nerve head drusen: improvements with spectral domain optical coherence tomography. *J Glaucoma* 2009;18:373-378.
86. Chen TC, Zeng A, Sun W, Mujat M, de Boer JF. Spectral domain optical coherence tomography in glaucoma. *Int Ophthalmol Clin* 2008;48:29-45.

87. Leitgeb R, Schmetterer L, Drexler W, et al. Real-time assessment of retinal blood flow with ultrafast acquisition by color doppler Fourier domain optical coherence tomography. *Opt Express* 2003;11:3116-3121.
88. Radhakrishnan S, Goldsmith J, Huang D, et al. Comparison of optical coherence tomography and ultrasound biomicroscopy for detection of narrow anterior chamber angles. *Arch Ophthalmol* 2005;123:1053-1059.
89. Sarunic MV, Asrani S, Izatt JA. Imaging the ocular anterior segment with real-time, full-range Fourier-domain optical coherence tomography. *Arch Ophthalmol* 2008;126:537-542.
90. Asrani S, Sarunic M, Santiago C, Izatt J. Detailed visualization of the anterior segment using Fourier-domain optical coherence tomography. *Arch Ophthalmol* 2008;126:765-771.
91. Christopoulos V, Kagemann L, Wollstein G, et al. In vivo corneal high-speed, ultra-high-resolution optical coherence tomography. *Arch Ophthalmol* 2007;125:1027-1035.
92. Cense B, Chen TC, Park BH, et al. In vivo birefringence and thickness measurements of the human retinal nerve fiber layer using polarization-sensitive optical coherence tomography. *J Biomed Opt* 2004;9:121-125.
93. Leitgeb RA, Hitzinger CK, Fercher AF, et al. Phase-shifting algorithm to achieve high-speed long-depth-range probing by frequency-domain optical coherence tomography. *Opt Lett* 2003;28:2201-2203.
94. Arnalich-Montiel F, Munoz-Negrete FJ, Rebolledo G, Sales-Sanz M, Cabarga C. Cup-to-disc ratio: agreement between slit-lamp indirect ophthalmoscopic estimation and stratus optical coherence tomography measurement. *Eye* 2007;21:1041-1049.
95. Martinez-De-La-Casa JM, Saenz-Frances F, Fernandez-Vidal AM, et al. Agreement between slit lamp examination and optical coherence tomography in estimating cup-disc ratios. *Eur J Ophthalmol* 2008;18:423-428.
96. Arthur SN, Aldridge AJ, De Leon-Ortega J, et al. Agreement in assessing cup-to-disc ratio measurement among stereoscopic optic nerve head photographs, HRTII, and Stratus OCT. *J Glaucoma* 2006;15:183-189.
97. Poli A, Strouthidis NG, Ho TA, Garway-Heath DF. Analysis of HRT images: comparison of reference planes. *Invest Ophthalmol Vis Sci* 2008;49:3970-3975.
98. Barkana Y, Harizman N, Gerber Y, Liebmann JM, Ritch R. Measurements of optic disk size with HRTII, Stratus OCT, and funduscopy are not interchangeable. *Am J Ophthalmol* 2006;142:375-380.
99. Hoffman EM, Bowd C, Medeiros FA, et al. Agreement among 3 optical imaging methods for the assessment of optic disc topography. *Ophthalmology* 2005;112:2149-2156.
100. Lamoureux EL, Lo K, Ferraro JG, et al. The agreement between the Heidelberg Retina Tomograph and a digital nonmydriatic retinal camera in assessing area cup-to-disc ratio. *Invest Ophthalmol Vis Sci* 2006;47:93-98.
101. Medeiros FA, Zangwill LM, Bowd C, Vasile C, Sample PA, Weinreb RN. Agreement between stereophotographic and confocal scanning laser ophthalmoscopy measurements of cup/disc ratio: effect on a predictive model for glaucoma development. *J Glaucoma* 2007;16:209-214.
102. Hitzl W, Hornykewycz K, Grabner G, Reitsamer HA. The cup-to-disc ratio: a comparison of TopSS, HRTII and subjective findings. *Klin Monatsbl Augenheilkd* 2007;224:391-395.
103. Jayasundera T, Danesh-Meyer HV, Donaldson M, Gamble G. Agreement between stereoscopic photographs, clinical assessment, Heidelberg retina tomograph and digital stereoscopic optic disc camera in estimating vertical cup:disc ratio. *Clin Experiment Ophthalmol* 2005;33:259-263.
104. Sung VC, Bhan A, Vernon SA. Agreement in assessing optic discs with a digital stereoscopic optic disc camera (Discam) and Heidelberg retina tomograph. *Br J Ophthalmol* 2002;86:196-202.
105. Povazay B, Hofer B, Hermann B, et al. Minimum distance mapping using three-dimensional optical coherence tomography for glaucoma diagnosis. *J Biomed Opt* 2007;12:041204.
106. Chen TC, Cense B, Miller JW, et al. Histologic correlation of in vivo optical coherence tomography images of the human retina. *Am J Ophthalmol* 2006;141:1165-1168.
107. American National Standards Institute. American National Standard for Safe Use of Lasers, ANSI Z136.1-2000, Orlando, Florida: Laser Institute of America; 2000.
108. Johnson CA, Keltner JL, Cello KE, et al. Baseline visual field characteristics in the Ocular Hypertension Treatment Study. *Ophthalmology* 2002;109:432-437.
109. Keltner JL, Johnson CA, Cello KE, et al. Classification of visual field abnormalities in the Ocular Hypertension Treatment Study. *Arch Ophthalmol* 2003;121:643-650.
110. Kass MA, Heuer DK, Higginbotham EJ, et al. The Ocular Hypertension Treatment Study: a randomized trial determines that topical ocular hypotensive medication delays or prevents the onset of primary open-angle glaucoma. *Arch Ophthalmol* 2002;120:701-713.
111. Smith M, Frost A, Graham CM, Shaw S. Effect of pupillary dilatation on glaucoma assessments using optical coherence tomography. *Br J Ophthalmol* 2007;91:1686-1690.
112. Savini G, Zanini M, Barboni P. Influence of pupil size and cataract on retinal nerve fiber layer thickness measurements by Stratus OCT. *J Glaucoma* 2006;15:336-340.
113. Stein DM, Wollstein G, Ishikawa H, et al. Effect of corneal drying on optical coherence tomography. *Ophthalmology* 2006;113:985-991.
114. Cheung CYL, Leung CKS, Lin D, Pang CP, Lam DSC. Relationship between retinal nerve fiber layer measurement and signal strength in optical coherence tomography. *Ophthalmology* 2008;115:1347-1351.

115. Wu Z, Vazeen M, Varma R, et al. Factors associated with variability in retinal nerve fiber layer thickness measurements obtained by optical coherence tomography. *Ophthalmology* 2007;114:1505-1512.
116. Yi K, Chen TC, de Boer JF. Spectral domain optical coherence tomography. *Tech Ophthalmol* 2006;4:170-174.
117. Yi K, de Boer JF, Chen TC. Optic nerve head and retinal nerve fiber layer imaging in glaucoma. *Contemp Ophthalmol* 2007;6:1-7.
118. Fercher AF, Hitzenberger CK, Kamp G, et al. Measurement of intraocular distances by backscattering spectral interferometry. *Opt Commun* 1995;117:43-48.
119. Leitgeb R, Hitzenberger CK, Fercher AF. Performance of Fourier domain vs time domain optical coherence tomography. *Opt Express* 2003;11:889-894.
120. Yun JW, Tearney GJ, de Boer JF, et al. Pulsed-source and swept-source spectral domain optical coherence tomography with reduced motion artifacts. *Opt Express* 2004;12:5614-5624.
121. Zhang Y, Cense B, Rha J, et al. High-speed volumetric imaging of cone photoreceptors with adaptive optics spectral-domain optical coherence tomography. *Opt Express* 2006;14:4380-4394.
122. Zawadzki RJ, Choi SS, Jones SM, Oliver SS, Werner JS. Adaptive optics-optical coherence tomography; optimizing visualization of microscopic retinal structures in three dimensions. *J Opt Soc Am A Opt Image Sci Vis* 2007;24:1373-1383.
123. Doble N. High-resolution, in vivo retinal imaging using adaptive optics and its future role in ophthalmology. *Expert Rev Med Devices* 2005;2:205-216.
124. Zawadzki RJ, Jones SM, Olivier SS, et al. Adaptive-optics optical coherence tomography for high-resolution and high-speed 3D retinal in vivo imaging. *Opt Express* 2005;13:8532-8546.
125. Hermann B, Fernandez EJ, Unterhuber A, et al. Adaptive-optics ultrahigh-resolution optical coherence tomography. *Opt Lett* 2004;29:2142-2144.
126. Minckler DS, McLean IW, Tso MO. Distribution of axonal and glial elements in the rhesus optic nerve head studied by electron microscopy. *Am J Ophthalmol* 1976;82:179-187.
127. Allingham RR, Damji KF, Freedman S, et al. Optic nerve, retina, and choroids. In: Allingham RR, Damji KF, Freedman S, Moroi SE, Shafranov G, eds. *Shields' Textbook of Glaucoma*. Philadelphia: Lippincott Williams & Wilkins; 2005:73-115.
128. Budenz DL, Chang RT, Huang X, Knighton RW, Tielsch JM. Reproducibility of retinal nerve fiber thickness measurements using the Stratus OCT in normal and glaucomatous eyes. *Invest Ophthalmol Vis Sci* 2005;46:2440-2443.
129. Budenz DL, Fredette MJ, Feuer WJ, Anderson DR. Reproducibility of peripapillary retinal nerve fiber thickness measurements with Stratus OCT in glaucomatous eyes. *Ophthalmology* 2008;115:661-666.
130. Shuman JS, Pedut-Kloizman T, Pakter H, et al. Optical coherence tomography and histologic measurements of nerve fiber layer thickness in normal and glaucomatous monkey eyes. *Invest Ophthalmol Vis Sci* 2007;48:3645-3654.
131. Gabriele ML, Ishikawa H, Wollstein G, et al. Optical coherence tomography scan circle location and mean retinal nerve fiber layer measurement variability. *Invest Ophthalmol Vis Sci* 2008;49:2315-2321.
132. Lu AT, Wang M, Varma R, et al. Combining nerve fiber layer parameters to optimize glaucoma diagnosis with optical coherence tomography. *Ophthalmology* 2008;115:1352-1357.
133. Leder DE, Schuman JS, Hertzmark E, et al. Analysis of macular volume in normal and glaucomatous eyes using optical coherence tomography. *Am J Ophthalmol* 2003;135:838-843.
134. Guedes V, Schuman JS, Hertzmark E, et al. Optical coherence tomography measurement of macular and nerve fiber layer thickness in normal and glaucomatous human eyes. *Ophthalmology* 2003;110:177-189.
135. Bowd C, Hao J, Tavares IM, et al. Bayesian machine learning classifiers for combining structural and functional measurements to classify healthy and glaucomatous eyes. *Invest Ophthalmol Vis Sci* 2008;49:945-953.
136. Hong S, Ahn H, Ha SJ, et al. Early glaucoma detection using the Humphrey Matrix perimeter, GDxVCC, Stratus OCT, and retinal nerve fiber layer photography. *Ophthalmology* 2007;114:210-215.
137. Lu AT, Wang M, Varma R, et al. Combining nerve fiber layer parameters to optimize glaucoma diagnosis with optical coherence tomography. *Ophthalmology* 2008;115:1352-1357.